The Aeronautical Journal (2026), **130**, pp. 1083–1106
doi:10.1017/aer.2025.10121

ROYAL AERONAUTICAL SOCIETY

RESEARCH ARTICLE

Neural network disturbance observer-based anti-saturation backstepping control for hypersonic vehicles

C. Wang[1], D. Feng[1], J. Zhao[3], P. Dai[1], T. Chen[1] and X. Wang[2]

[1]School of Aerospace Science and Technology, Xidian University, Xi'an, China
[2]School of Astronautics, Northwestern Polytechnical University, Xi'an, China
[3]Beijing System Design Institute of Electro Mechanic Engineering, Beijing, China
Corresponding author: P. Dai; Email: daipei@xidian.edu.cn

Received: 16 January 2025; **Revised:** 9 December 2025; **Accepted:** 10 December 2025

Keywords: adaptive fixed-time anti-saturation compensator; anti-saturation backstepping controller; hypersonic vehicles; neural network disturbance observers

Abstract

This study proposes a radial basis function neural network disturbance observer- (RBFNNDO) based anti-saturation backstepping controller for hypersonic vehicles with input saturations and multiple disturbances. Firstly, in response to the problem of 'exploding complexity' in backstepping controller, we adopt finite-time tracking differentiators (FTD), which realise higher tracking accuracy and tracking speed than those of the existing methods. Secondly, we develop multivariable neural network disturbance observers to estimate the lumped disturbances involving aerodynamic uncertainties and external disturbances, thereby improving the robustness of the proposed controller. Thirdly, in order to alleviate the input saturation and minimise the duration time, we use an adaptive fixed-time anti-saturation compensator (AFAC). The simulation results have proven that our proposed backstepping controller outperforms other existing methods in terms of control performance and saturation time.

Nomenclature

α	angle-of-attack, degree
β	sideslip angle, degree
μ	bank angle, degree
p	roll rate, degree·s^{-1}
q	pitch rate, degree·s^{-1}
r	yaw rate, degree·s^{-1}
δ_a	right elevon angular deflection, degree
δ_e	left elevon angular deflection, degree
δ_r	rudder angular deflection, degree
Q	dynamic pressure, pa
S	reference area, ft^2
b	lateral-directional reference length, ft
c	longitudinal reference length, ft
$C_l^{\delta a}$	rolling moment increment coefficient for right elevon
$C_l^{\delta e}$	rolling moment increment coefficient for left elevon
$C_l^{\delta r}$	rolling moment increment coefficient for rudder
$C_m^{\delta a}$	pitching moment increment coefficient for right elevon
$C_m^{\delta e}$	pitching moment increment coefficient for left elevon
$C_m^{\delta r}$	pitching moment increment coefficient for rudder
$C_n^{\delta a}$	yawing moment increment coefficient for right elevon

© The Author(s), 2026. Published by Cambridge University Press on behalf of Royal Aeronautical Society.

https://doi.org/10.1017/aer.2025.10121 Published online by Cambridge University Press

$C_n^{\delta e}$	yawing moment increment coefficient for left elevon
$C_n^{\delta r}$	yawing moment increment coefficient for rudder
C_L^{α}	lift increment coefficient for α
C_Y^{β}	side force coefficient for β
$C_L^{\delta a}$	lift increment coefficient for right elevon
$C_L^{\delta e}$	lift increment coefficient for left elevon
$C_Y^{\delta r}$	side force increment coefficient for rudder
I_x, I_y, I_z	roll, pitch and yaw moments of inertia respectively, slg-ft^2
AFAC	adaptive fixed-time anti-saturation compensator
DO	disturbance observer
ESD	Oextend state disturbance observer
FTD	finite-time tracking differentiator
HFV	hypersonic flight vehicle
NDO	nonlinear disturbance observer
NN	neural network
NN-ABC	NN-based anti-saturation backstepping control
PSMC	predictive sliding mode control
RBFNNDO	radial basis function neural network disturbance observer

1.0 Introduction

Hypersonic flight vehicle (HFV) can fly faster than Mach 5 with its altitude typically ranging from 20 to 100 km [1, 2], and its time-varying dynamic model is also featured with the characteristics of strong coupling, nonlinearity and multisource uncertainties. The above characteristics pose great challenges to the designing of HFV controllers [3, 4]. Unfortunately, the linear flight control methods for HFVs have certain limitations, for which reason related studies on nonlinear control methods are required for HFVs. In recent years, most of the existing studies primarily focused on nonlinear control methods such as backstepping control [5, 6], sliding mode control [7–9], intelligent control [10, 11], adaptive control [12, 13], fault tolerant control [14], etc.

The backstepping control method is a typical nonlinear approach based on Lyapunov stability control theory. The backstepping control method has been widely applied in various research fields. In 2019, Sun et al. developed nonsmooth backstepping controllers for the altitude and velocity subsystems to achieve a fixed-time convergence [15]. This approach is capable of filtering out noises and acquiring uncertainty estimations while ensuring tracking accuracy. Later in 2022, Zhao et al. [16] proposed a decentralised actuator fault compensation scheme for HFV using model transformation based backstepping control method. It must be noted that backstepping control requires calculating the derivative of virtual control signal, which may result in explosion of complexity [17]. In order to solve the above problem, command filters are utilised to approximate the output of the filter to the derivative of the virtual control variable [18–20]. It is known that the command-filter-based backstepping control method can only ensure that the system is bounded, the convergence region may still be affected by the tracking error of the filter.

Since the control system is susceptible to external disturbances and uncertainties, the technology of disturbance observer (DO) has been developed to enable anti-disturbance capability for the controller. Researchers use disturbance observers to compensate for tracking errors brought by external disturbances and to ensure the stability and dynamic performance of the closed-loop dynamic system. In 2012, Zong et al. investigated a hybrid control framework that combined a nonlinear disturbance observer (NDO) with backstepping for controlling the flight of HFV [21]. Cheng et al. proposed a new disturbance suppression scheme in 2017 to address the problem of uncertainty, which firstly used predictive sliding mode control (PSMC) to reduce the mismatch model uncertainty of the outer loop subsystem, and then proposed a PSMC based on NDO to solve the mismatch disturbance problem of the inner loop subsystem [22]. Subsequently, Wang et al. designed a non-singular fast terminal sliding mode controller based on finite time NDO to eliminate disturbance observation and trajectory errors [23]. Neural network (NN) is also an effective approach for eliminating disturbances due to its excellent uncertainty

https://doi.org/10.1017/aer.2025.10121 Published online by Cambridge University Press

approximation capabilities [24]. Bu et al. utilised fuzzy wavelet neural networks to estimate unknown flight dynamics to guarantee the robustness of hybrid controllers. Based upon deep belief network [25], Sun et al. proposed a semi-supervised controller in the presence of unknown external disturbances [26]. Although the existing studies achieve uncertainty estimation, there remains a lack of effort in reducing the computational overhead of neural approximation.

When the actuator of HFV is unable to follow the growth control law due to physical limitations during flight, the saturation will occur, which will cause the misfunction of HFV controller and produce severe consequences [27]. Currently, the prevailing anti-saturation methods include one-step approach [28, 29] and anti-saturation compensation approach [30, 31]. The former is relatively conservative and may restrict the performance of the controller, whereas the latter introduces an anti-saturation compensator in the nominal controller. Despite that introducing auxiliary variable into the compensator can quickly release the actuator from saturation while ensuring system stability, however, the presence of auxiliary variable can affect the convergence characteristics of the nominal controller. In addition, adopting general nominal compensators only make the auxiliary variable converge asymptotically or exponentially.

In this study, we design a novel RBFNNDO-based anti-saturation backstepping controller for HFVs with input saturations. We introduce a novel finite-time tracking differentiator (FTD) to compute derivatives of virtual control laws and flow angle commands, offering higher accuracy compared to traditional command filters. Furthermore, considering the universal approximation characteristics of radial basis function neural networks (RBFNN), we design an adaptive RBFNN disturbance observer (RBFNNDO) to approximate and compensate for the total disturbances of the system. In addition, we adopt a new type of adaptive fixed-time anti-saturation compensator (AFAC) [32] to make that the auxiliary variables have a fixed-time convergence. The key contributions of this study can be summarised as follows.

Firstly, we establish a 6-degrees-of-freedom (6-DOF) control-oriented HFV model with input saturations and uncertain disturbances, to which the forms of input saturations and the specific equations for uncertain disturbance terms are presented.

Secondly, compared to the extended state disturbance observer (ESDO) presented in Ref. (35), we introduce a RBFNNDO to observe the total disturbance and compensate for it within the controller, which can enhance the accuracy of observation error.

Thirdly, in contrast to existing research, such as that presented in Ref. (31), which primarily concentrates on anti-saturation strategies for the longitudinal model of hypersonic vehicles, the multivariable compensator employed in this study offers a significant advancement. This compensator is capable of simultaneously mitigating the saturation effects across three actuators and exhibits a fixed-time convergence characteristic.

The remainder of this paper is organised as follows. Section 2 introduces a control-oriented model of HFV. Section 3 highlights the design of NN-ABC, including the design of RBFNNDO, FTD and AFAC, presenting stability analysis for the controller. Section 4 designs comparative simulation experiments and provides corresponding results, by which the performance of our proposed method has been verified. Section 5 summarises conclusions of this study and outlines our future research interest.

2.0 Problem description and preliminaries

2.1 HFV model

According to Refs [33–35], the control-oriented model for HFVs is denoted by

$$\begin{cases} \dot{\boldsymbol{\Omega}} = \boldsymbol{f}_{\boldsymbol{\Omega}} + \boldsymbol{g}_{\boldsymbol{\Omega}}\boldsymbol{\omega} + \boldsymbol{\Delta}_{\boldsymbol{\Omega}} \\ \dot{\boldsymbol{\omega}} = \boldsymbol{f}_{\boldsymbol{\omega}} + \boldsymbol{g}_{\boldsymbol{\omega}}\boldsymbol{u} + \boldsymbol{\Delta}_{\boldsymbol{\omega}} \end{cases}. \tag{1}$$

In (1), $\boldsymbol{\Omega} = [\alpha, \beta, \mu]^T$ denotes the vector of three flow angles, $\omega = [p, q, r]^T$ denotes the vector of three angular velocities, and $\boldsymbol{u} = [\delta_a, \delta_e, \delta_r]^T$ denotes the vector of three-channel control inputs, $\boldsymbol{\Delta}_{\boldsymbol{\Omega}}$ and $\boldsymbol{\Delta}_{\boldsymbol{\omega}}$ denote the disturbances in flow angles and angular velocities, respectively. $\boldsymbol{g}_{\boldsymbol{\Omega}}$ and $\boldsymbol{g}_{\boldsymbol{\omega}}$ can be expressed as

https://doi.org/10.1017/aer.2025.10121 Published online by Cambridge University Press

$$\boldsymbol{g}_{\boldsymbol{\Omega}}=\begin{bmatrix}-\tan\beta\cos\alpha & 1 & -\tan\beta\sin\alpha\\ \sin\alpha & 0 & -\cos\alpha\\ \sec\beta\cos\alpha & 0 & \sec\beta\sin\alpha\end{bmatrix},\boldsymbol{g}_{\boldsymbol{\omega}}=\begin{bmatrix}\frac{QSbC_l^{\delta a}}{I_x} & \frac{QSbC_l^{\delta e}}{I_x} & \frac{QSbC_l^{\delta r}}{I_x}\\ \frac{QScC_m^{\delta a}}{I_z} & \frac{QScC_m^{\delta e}}{I_z} & \frac{QScC_m^{\delta r}}{I_z}\\ \frac{QSbC_n^{\delta a}}{I_y} & \frac{QSbC_n^{\delta e}}{I_y} & \frac{QSbC_n^{\delta r}}{I_y}\end{bmatrix} \tag{2}$$

$\boldsymbol{f}_{\boldsymbol{\Omega}}$ and $\boldsymbol{f}_{\boldsymbol{\omega}}$ can be expressed as

$$\boldsymbol{f}_{\boldsymbol{\Omega}}=\begin{bmatrix}\frac{mg\cos\mu\cos\theta-QSC_L^{\alpha}}{mV_b\cos\beta}\\ \frac{mg\cos\theta\sin\mu+QSC_Y^{\beta}\beta\cos\beta}{mV_b}\\ \frac{-mg\cos\mu\cos\theta\tan\beta+QS\begin{bmatrix}C_L^{\alpha}\tan\theta\sin\mu+C_L^{\alpha}\tan\beta\\ +C_Y^{\beta}\beta\cos\beta\tan\theta\cos\mu\end{bmatrix}}{mV_b}\end{bmatrix},\boldsymbol{f}_{\boldsymbol{\omega}}=\begin{bmatrix}\frac{l_0-qr\left(I_z-I_y\right)}{I_x}\\ \frac{m_0-pr\left(I_x-I_z\right)}{I_y}\\ \frac{n_0-pq\left(I_y-I_x\right)}{I_z}\end{bmatrix}. \tag{3}$$

In (2) and (3), l_0, m_0 and n_0 represent the aerodynamic moments. m, θ denote the mass of aircraft and flight path angle, and the other variables in model are given in nomenclature. Then, the disturbances $\boldsymbol{\Delta}_{\boldsymbol{\Omega}}=[\Delta_\alpha,\Delta_\beta,\Delta_\mu]^T$ and $\boldsymbol{\Delta}_{\boldsymbol{\omega}}=[\Delta_p,\Delta_q,\Delta_r]^T$ can be expressed as

$$\begin{cases}\Delta_\alpha=-\dfrac{QS\left(C_L^{\delta a}+C_L^{\delta e}+\Delta C_L\right)}{mV_b\cos\beta}+d_\alpha\\ \Delta_\beta=\dfrac{QS\left(C_Y^{\delta r}\cos\beta+\Delta C_Y\right)}{mV_b}+d_\beta\\ \Delta_\mu=\dfrac{QS\left(C_L^{\delta a}+C_L^{\delta e}+\Delta C_L\right)\left(\tan\beta+\tan\theta\sin\mu\right)+\left(QS\left(C_Y^{\delta r}\cos\beta+\Delta C_Y\right)\right)\tan\theta\cos\mu}{mV_b}+d_\mu\\ \Delta_p=\Delta C_l qsb+d_p\\ \Delta_q=\Delta C_m qsc+d_q\\ \Delta_r=\Delta C_n qsb+d_r\end{cases}, \tag{4}$$

where $d_i(i=\alpha,\beta,\mu,p,q,r)$ represents the external disturbances.

The control input is bounded due to structural limitations, which is expressed as

$$u_i=sat\left(u_{ci}\right),\quad i=a,e,r. \tag{5}$$

In (5), $\boldsymbol{u}_c$ is the ideal command calculated by the control law. The deviation vector between the actual and ideal command of control input is defined as

$$\Delta\boldsymbol{u}=\boldsymbol{u}-\boldsymbol{u}_{\mathbf{c}} \tag{6}$$

2.2 Preliminaries

Consider the system of differential equations [39]

$$\dot{x}=f(t,x),x(0)=x_0 \tag{7}$$

where $x\in\mathbb{R}^n$ and $f:\mathbb{R}_+\times\mathbb{R}^n\to\mathbb{R}^n$ is a nonlinear function. Suppose the origin is an equilibrium point of (7).

https://doi.org/10.1017/aer.2025.10121 Published online by Cambridge University Press

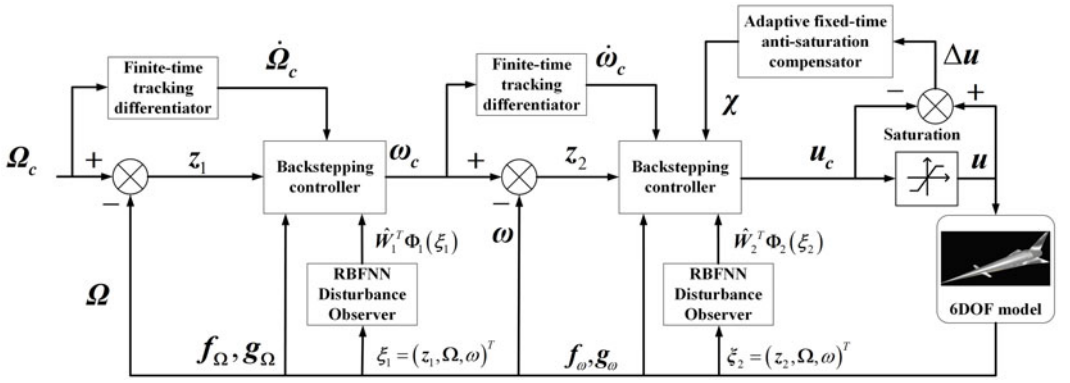


Figure 1. *Schematic diagram demonstrating the structure of NN-ABC controller.*

Definition 1. *The origin of (7) is said to be globally finite-time stable if it is globally asymptotically stable and any solution $x(t, x_0)$ of (7) reaches the origin at some finite moment, i.e., $x(t, x_0) = 0$, $\forall t \geq T(x_0)$, where $T : \mathbb{R}^n \to \mathbb{R}_+ \cup 0$ is the settling time function.*

Definition 2. *The origin (7) of is said to be fixed-time stable if it is globally finite-time stable and the settling time function $T(x_0)$ is bounded, i.e., $\exists T_{\max} > 0 : T(x_0) \leq T_{\max}, \forall x_0 \in \mathbb{R}^n$.*

Lemma 1. *Consider the following nonlinear system [34]*

$$\begin{cases} \dot{z}_1 = -\xi_1 sig^{\alpha_1}(z_1) + z_2 \\ \dot{z}_2 = -\xi_2 sig^{\alpha_2}(z_1) - p \end{cases}, \quad |p| \leq \bar{p}, \tag{8}$$

where $\xi_1, \xi_2 > 0$, $\alpha_1 \in (0.5, 1)$, $\alpha_2 = 2\alpha_1 - 1$, p is a bounded constant. The system defined in (8) is finite-time stable, the residual set of the solution D_0 and the settling time T_0 are bounded [35], which can be expressed by

$$\begin{aligned} D_0 &= \left\{ \varepsilon \mid V(\varepsilon) < \left(\frac{M_2}{\theta} \right)^{2\alpha_1/\alpha_2} \right\}, \theta \in (0, M_1) \\ T_0 &\leq \left[\frac{V(\boldsymbol{\varepsilon}_0)^{1-\sigma}}{(M_1 - \theta)(1-\sigma)} \right] \end{aligned}, \tag{9}$$

where $\sigma = (\alpha_1 + \alpha_2)/2\alpha_1$, and the definition of M_1 and M_2 can be found in Ref. (34).

Lemma 2. *Consider the following nonlinear system [35, 36]*

$$\dot{\sigma} = -k_1 sig^{q_1}(\sigma) - k_2 sig^{q_2}(\sigma), \sigma(0) = \sigma_0, \tag{10}$$

where $0 < q_1 < 1$, $q_2 > 1$, $k_1, k_2 > 0$, $sig^q(\sigma)$ denotes $[|\sigma_1|^q \operatorname{sign}(\sigma_1), \cdots, |\sigma_n|^q \operatorname{sign}(\sigma_n)]^T$. The system given by (7) exhibits fixed-time stability [35], and the settling time $T(\sigma_0)$ is bounded, which can be expressed by

$$T(\sigma_0) \leq T_{\max} = \frac{1}{k_1(1-q_1)} + \frac{1}{k_2(q_2-1)}. \tag{11}$$

3.0 Controller law design and stability assessment

The configurations of NN-ABC controllers are described in detail in the following five sections. The structure of NN-ABC is demonstrated in Fig. 1.

https://doi.org/10.1017/aer.2025.10121 Published online by Cambridge University Press

3.1 Designing neural network disturbance observer

The RBFNN can be designed as a disturbance observer to estimate the unknown and bounded function $D(x) \in R^m$ [37], which can be expressed as

$$D(\boldsymbol{x}) = \boldsymbol{W}^{*T}\Phi(\boldsymbol{x}) + \boldsymbol{\varepsilon} \tag{12}$$

In (12), $\boldsymbol{\varepsilon} \in R^m$ represents the approximation error vector, $\boldsymbol{W}^* \in R^{n\times m}$ represents the ideal weight matrix and is designed as

$$\boldsymbol{W}^* = \arg\min_{\hat{W}} \left\{ \sup_{x\in R^a} \left| D(x) - \boldsymbol{W}^T \Phi(x) \right| \right\}. \tag{13}$$

In (13), $\hat{W}$ denotes the estimate of $\boldsymbol{W}^*$, $x \in R^a$ denotes the input vector, $n\ (>1)$ denotes the number of neural network neurons (nodes), $\Phi(\mathbf{x}) = [\boldsymbol{\Phi}_1(\boldsymbol{x}), \boldsymbol{\Phi}_2(\boldsymbol{x}), \ldots \Phi_n(\boldsymbol{x})]^T$ denotes the radial basis function vector, $\Phi_i(x)$ denotes the output of the i-th Gaussian function expressed by

$$\Phi_i(x) = \exp\left(-\frac{\|x - \sigma_i\|^2}{2b_i^2} \right). \tag{14}$$

In (14), $\sigma_i \in R^n$ and $b_i > 0$ denote the centre and the width of this Gaussian function, respectively.

In this case, two RBFNN disturbance observers are designed to estimate the lumped disturbances in (1), which are expressed as

$$\begin{aligned} \boldsymbol{\Delta}_{\boldsymbol{\Omega}} &= \boldsymbol{W}_1{}^{*T}\boldsymbol{\Phi}_1\left(\boldsymbol{\xi}_1\right) + \boldsymbol{\varepsilon}_1 \\ \boldsymbol{\Delta}_{\boldsymbol{\omega}} &= \boldsymbol{W}_2{}^{*T}\boldsymbol{\Phi}_2\left(\boldsymbol{\xi}_2\right) + \boldsymbol{\varepsilon}_2 \end{aligned}, \tag{15}$$

where $\boldsymbol{W}_1{}^*$ and $\boldsymbol{W}_2{}^* \in R^{n\times 3}$ denote the ideal weight matrices, ξ_1 and ξ_2 denote the input vectors to be designed, $\boldsymbol{\varepsilon}_1$ and $\boldsymbol{\varepsilon}_2 \in R^{3\times 1}$ denote the approximation error vectors.

Remark 1. Owing to the finite dimensional hidden layer of the RBFNN, the approximation error exists [37]. Besides, the approximation errors $\boldsymbol{\varepsilon}_1$ and $\boldsymbol{\varepsilon}_2$ can be bounded when appropriate number of neurons and appropriate centre and width of the Gaussian function are selected.

Remark 2. In order to enhance the estimation accuracy and performance effectiveness of the RBFNN in identifying and accurately quantifying system perturbations, this study adopts the system error term, the internal state variable and the external excitation signal to form the input feature vector.

3.2 Finite-time tracking differentiator design

Assumption 1. Considering engineering practice, assume the flow angle commands be $\boldsymbol{\Omega}_c$, the virtual control signals be $\boldsymbol{\omega}_c$, and their second derivatives are bounded.

In this subsection, FTDs are designed to approximate the derivatives of flow angle commands and virtual control signals, which can be expressed as

$$\begin{cases} \dot{\hat{\boldsymbol{\Omega}}}_c(t) = \boldsymbol{\lambda_1}(t) - l_1 sig^{\alpha_1}\left(\hat{\boldsymbol{\Omega}}_c - \boldsymbol{\Omega}_c\right), \ \boldsymbol{\Omega}_c = (\alpha_{cmd}, \beta_{cmd}, \mu_{cmd}) \\ \dot{\boldsymbol{\lambda}}_{\mathbf{1}}(t) = -l_2 sig^{\alpha_2}\left(\hat{\boldsymbol{\Omega}}_c - \boldsymbol{\Omega}_c\right) \\ \dot{\hat{\boldsymbol{\omega}}}_c(t) = \boldsymbol{\lambda_2}(t) - l_3 sig^{\beta_1}\left(\hat{\boldsymbol{\omega}}_c - \boldsymbol{\omega}_c\right), \ \boldsymbol{\omega}_c = (p_{cmd}, q_{cmd}, r_{cmd}) \\ \dot{\boldsymbol{\lambda}}_{\mathbf{2}}(t) = -l_4 sig^{\beta_2}\left(\hat{\boldsymbol{\omega}}_c - \boldsymbol{\omega}_c\right) \end{cases}, \tag{16}$$

where $l_i > 0\ (i = 1, \ldots, 4)$, $\alpha_1, \beta_1 \in (0.5, 1)$, $\alpha_2 = 2\alpha_1 - 1$, $\beta_2 = 2\beta_1 - 1$, $\boldsymbol{\lambda_1}$ and $\boldsymbol{\lambda_2}$ represent the derivatives of the flow angle commands and virtual control laws estimated by the two FTDs indicated in (16).

Theorem 1. *The derivatives of $\boldsymbol{\Omega}_c$ and $\boldsymbol{\omega}_c$ can be precisely approximated by the FTDs designed in (16) in finite time, based upon which the approximation errors will converge to a small region near the origin.*

https://doi.org/10.1017/aer.2025.10121 Published online by Cambridge University Press

Proof: The error variables of FTDs can be defined as

$$\begin{cases} \boldsymbol{E_1} = \hat{\boldsymbol{\Omega}}_c - \boldsymbol{\Omega}_c \\ \boldsymbol{E}_2 = \boldsymbol{\lambda_1} - \dot{\boldsymbol{\Omega}}_c \end{cases}, \quad \begin{cases} \boldsymbol{E}_3 = \hat{\boldsymbol{\omega}}_c - \boldsymbol{\omega}_c \\ \boldsymbol{E}_4 = \boldsymbol{\lambda_2} - \dot{\boldsymbol{\omega}}_c \end{cases} \tag{17}$$

The error dynamic system can be obtained by differentiating both sides of (17), which can be written as

$$\begin{cases} \dot{\boldsymbol{E}}_1 = -l_1 sig^{\alpha_1}(\boldsymbol{E_1}) + \boldsymbol{E_2} \\ \dot{\boldsymbol{E}}_2 = -l_2 sig^{\alpha_2}(\boldsymbol{E_1}) - \ddot{\boldsymbol{\Omega}}_c \end{cases}, \quad \begin{cases} \dot{\boldsymbol{E}}_3 = -l_3 sig^{\beta_1}(\boldsymbol{E}_3) + \boldsymbol{E}_4 \\ \dot{\boldsymbol{E}}_4 = -l_4 sig^{\beta_2}(\boldsymbol{E}_3) - \ddot{\boldsymbol{\omega}}_c \end{cases} \tag{18}$$

The approximation errors $\boldsymbol{E}_i$ $(i = 1, 2, 3, 4)$ can converge to a small region near the origin in finite time according to **Lemma 1**. In other words, the derivatives of the flow angle commands and virtual control signals can be precisely approximated within finite time, thereby validating the proof.

3.3 Designing adaptive fixed-time anti-saturation compensator

The AFAC [32, 35] is introduced to deal with the problem of input saturations, which is expressed as

$$\dot{\boldsymbol{\chi}} = -k_{\chi 1} L_\chi sig^{a_{\chi 1}}(\boldsymbol{\chi}) - k_{\chi 2} L_\chi sig^{a_{\chi 2}}(\boldsymbol{\chi}) + \boldsymbol{g}_\omega \boldsymbol{\Delta} u, \tag{19}$$

where $a_{\chi 1} \in (0, 1)$, $a_{\chi 2} > 1$, $k_{\chi 1} > 0$, $k_{\chi 2} > 0$, and $\chi = [\chi_1 \chi_2 \chi_3]^T$ denotes the auxiliary variable introduced in the angular rate loop, which can be used in the control law calculation in the following subsection 3.4. The L_χ denotes the positive adaptive gain [35], and the adaptive law of L_χ can be described by

$$\dot{L}_\chi = \begin{cases} -k_{L\chi 1} L_\chi - k_{L\chi 2} L_\chi^{\frac{1}{2}} + k_{L\chi 1} P^L, & \boldsymbol{\Delta} u \neq 0 \\ Proj_{L_\chi}\left(k_{L\chi 3} L_\chi^{a_{L\chi 1}} + k_{L\chi 4} L_\chi^{-a_{L\chi 2}} + c_L\right), & \boldsymbol{\Delta} u = 0 \end{cases}$$

$$Proj_{L_\chi}(\bullet) = \begin{cases} 0 & \text{if} \quad L_\chi = P^U \quad \text{and} \quad \bullet \geq 0 \\ 0 & \text{if} \quad L_\chi = P^L \quad \text{and} \quad \bullet \leq 0 \\ \bullet & \text{otherwise} \end{cases} \tag{20}$$

where $k_{L\chi 1}$, $k_{L\chi 2}$, $k_{L\chi 3}$, $k_{L\chi 4}$, $a_{L\chi 1}$, $a_{L\chi 2}$ and c_L denote the positive design parameters, P^U and P^L denote the upper and lower bounds of L_χ, respectively. Detailed explanations and discussions can be found in Refs [32] and [35].

3.4 Controller law design

Step 1: Define the deviation variable of the command variables as $\boldsymbol{z_1} = \boldsymbol{\Omega} - \boldsymbol{\Omega}_c$, and its derivative is determined by

$$\dot{\boldsymbol{z}}_1 = \dot{\boldsymbol{\Omega}} - \dot{\boldsymbol{\Omega}}_c = f_{\boldsymbol{\Omega}} + \boldsymbol{g}_{\boldsymbol{\Omega}} \boldsymbol{\omega} + \boldsymbol{\Delta}_{\boldsymbol{\Omega}} - \dot{\boldsymbol{\Omega}}_c. \tag{21}$$

Therefore, the virtual control law for angular rates to track is established as

$$\boldsymbol{\omega}_c = \boldsymbol{g}_{\boldsymbol{\Omega}}^{-1}\left(-K_1 \boldsymbol{z_1} - f_{\boldsymbol{\Omega}} - \hat{\boldsymbol{W}}_1^T \boldsymbol{\Phi}_1(\boldsymbol{\xi}_1) + \boldsymbol{\lambda_1}\right), \tag{22}$$

https://doi.org/10.1017/aer.2025.10121 Published online by Cambridge University Press

where K_1 denotes a positive parameter, $\hat{\boldsymbol{W}}_1$ denotes the estimation of the ideal weight matrix $\boldsymbol{W}_1{}^*$, $\xi_1 = (z_1, \boldsymbol{\Omega}, \boldsymbol{\omega})^T$ denotes the input vector of the RBFNN, $\boldsymbol{\lambda_1}$ represents the estimation of $\dot{\boldsymbol{\Omega}}_c$ produced by the finite-time tracking differentiators described in. The adaptive weight update law of $\hat{\boldsymbol{W}}_1$ is designed as

$$\dot{\hat{\boldsymbol{W}}}_1 = \Gamma_1 \boldsymbol{\Phi}_1 \left(\boldsymbol{\xi}_1\right) \boldsymbol{z_1}^T, \tag{23}$$

where Γ_1 is a positive parameter to be designed.

Substituting (22) into (21), we obtain

$$\dot{\boldsymbol{z}}_1 = -K_1 \boldsymbol{z_1} + \boldsymbol{g}_{\boldsymbol{\Omega}} \boldsymbol{z_2} + \tilde{\boldsymbol{W}}_1^T \boldsymbol{\Phi}_1 \left(\boldsymbol{\xi}_1\right) + \boldsymbol{\varepsilon}_1 + \tilde{\dot{\boldsymbol{\Omega}}}_c, \tag{24}$$

where $\tilde{\boldsymbol{W}}_1 = \boldsymbol{W}_1{}^* - \hat{\boldsymbol{W}}_1$ and $\tilde{\dot{\boldsymbol{\Omega}}}_c = \boldsymbol{\lambda_1} - \dot{\boldsymbol{\Omega}}_c$.

Step 2: Define the deviation variable between the real and ideal angular rates as $\boldsymbol{z_2} = \omega - \boldsymbol{\omega}_c$. Therefore, the augmented deviation variable y containing auxiliary variable in (19) is defined as

$$\boldsymbol{y} = \boldsymbol{z_2} - \chi. \tag{25}$$

Differentiating both sides (25) of and substituting (19) and (6) into (25), we obtain

$$\begin{aligned} \dot{\boldsymbol{y}} = \dot{\boldsymbol{z}}_2 - \dot{\boldsymbol{\chi}} &= \boldsymbol{f}_{\boldsymbol{\omega}} + \boldsymbol{g}_{\boldsymbol{\omega}} u + \boldsymbol{\Delta}_{\omega} - \dot{\boldsymbol{\omega}}_c + k_{\chi 1} L_{\chi} sig^{a_{\chi 1}} (\boldsymbol{\chi}) + k_{\chi 2} L_{\chi} sig^{a_{\chi 2}} (\boldsymbol{\chi}) - \boldsymbol{g}_{\boldsymbol{\omega}} \boldsymbol{\Delta} u \\ &= \boldsymbol{f}_{\boldsymbol{\omega}} + \boldsymbol{g}_{\boldsymbol{\omega}} \boldsymbol{u}_c + \boldsymbol{\Delta}_{\omega} - \dot{\boldsymbol{\omega}}_c + k_{\chi 1} L_{\chi} sig^{a_{\chi 1}} (\boldsymbol{\chi}) + k_{\chi 2} L_{\chi} sig^{a_{\chi 2}} (\boldsymbol{\chi}) \end{aligned} \tag{26}$$

Furthermore, the control input $\boldsymbol{u}_c$ is designed as

$$\boldsymbol{u}_c = \boldsymbol{g}_{\boldsymbol{\omega}}{}^{-1} \left[-K_2 y - \boldsymbol{g}_{\boldsymbol{\Omega}}^T \boldsymbol{z_1} - \boldsymbol{f}_{\boldsymbol{\omega}} - \hat{W}_2^T \boldsymbol{\Phi}_2 \left(\boldsymbol{\xi}_2\right) + \boldsymbol{\lambda_2} - k_{\chi 1} L_{\chi} sig^{a_{\chi 1}} (\boldsymbol{\chi}) - k_{\chi 2} L_{\chi} sig^{a_{\chi 2}} (\boldsymbol{\chi}) \right], \tag{27}$$

where K_2 denotes a positive design parameter, $\hat{\boldsymbol{W}}_2$ denotes the estimation of the ideal weight matrix $\boldsymbol{W}_2{}^*$, $\xi_2 = (z_2, \boldsymbol{\Omega}, \boldsymbol{\omega})^T$ denotes the input vector, $\boldsymbol{\lambda_2}$ denotes the estimation of $\dot{\boldsymbol{\omega}}_c$ described in (16). The adaptive weight update law of $\hat{\boldsymbol{W}}_2$ is designed as

$$\dot{\hat{\boldsymbol{W}}}_2 = \Gamma_2 \boldsymbol{\Phi}_2 \left(\boldsymbol{\xi}_2\right) \boldsymbol{y}^T, \tag{28}$$

where Γ_2 is a positive parameter to be designed.

Substituting (27) into (26), we obtain

$$\dot{\boldsymbol{y}} = -K_2 y - \boldsymbol{g}_{\boldsymbol{\Omega}}^T \boldsymbol{z_1} + \tilde{\boldsymbol{W}}_2^T \boldsymbol{\Phi}_2 \left(\boldsymbol{\xi}_2\right) + \boldsymbol{\varepsilon}_2 + \tilde{\dot{\boldsymbol{\omega}}}_c, \tag{29}$$

where $\tilde{\boldsymbol{W}}_2 = \boldsymbol{W}_2{}^* - \hat{\boldsymbol{W}}_2$, $\tilde{\dot{\boldsymbol{\omega}}}_c = \boldsymbol{\lambda_2} - \dot{\boldsymbol{\omega}}_c$.

Remark 3. In the absence of saturation, the adaptive law increases the proportion of L_{χ}, reducing $\boldsymbol{\chi}$ to zero in fixed-time [32, 35]. Under this circumstance, the anti-saturation controller degenerates to the backstepping controller [32, 35].

$$T_a \leq \frac{1}{k_{\chi 1} L_{\chi} \left(1 - a_{\chi 1}\right)} + \frac{1}{k_{\chi 2} L_{\chi} \left(a_{\chi 2} - 1\right)} \tag{30}$$

3.5 Stability assessment

Theorem 2. *The auxiliary variable* $\boldsymbol{\chi}$ *brought in through the AFAC is bounded.*

Proof. The following Lyapunov function is selected as

$$V_1 = \frac{1}{2} \boldsymbol{\chi}^T \chi, \tag{31}$$

The time derivative of V_1 is $\dot{V}_1 = \boldsymbol{\chi}^T \left(-k_{\chi 1} L_{\chi} sig^{a_{\chi 1}} (\boldsymbol{\chi}) - k_{\chi 2} L_{\chi} sig^{a_{\chi 2}} (\boldsymbol{\chi}) + \boldsymbol{g}_{\boldsymbol{\omega}} \boldsymbol{\Delta} u\right)$.

Assume the control law $\boldsymbol{u}_c$ in (27) is bounded. Under these circumstances, a positive constant u_M exists, with $\Delta u_i \leq u_M$, $(i = a, e, r)$ and $M = [\, u_M \;\; u_M \;\; u_M \,]^T$. Therefore, we have

https://doi.org/10.1017/aer.2025.10121 Published online by Cambridge University Press

$$\begin{aligned}\dot{V}_1 &\le \boldsymbol{\chi}^T\left(-k_{\chi 1}L_\chi sig^{a_{\chi 1}}(\boldsymbol{\chi})-k_{\chi 2}L_\chi sig^{a_{\chi 2}}(\boldsymbol{\chi})+\boldsymbol{g}_\omega\boldsymbol{\Delta u}\right)\\ &=-k_{\chi 1}L_\chi\left(|\chi_1|^{1+a_{\chi 1}}+|\chi_2|^{1+a_{\chi 1}}+|\chi_3|^{1+a_{\chi 1}}\right)-k_{\chi 2}L_\chi\left(|\chi_1|^{1+a_{\chi 2}}+|\chi_2|^{1+a_{\chi 2}}+|\chi_3|^{1+a_{\chi 2}}\right)+\boldsymbol{\chi}^T\boldsymbol{g}_\omega\boldsymbol{\Delta u}\\ &\le -k_{\chi 1}L_\chi\left(|\chi_1|^{1+a_{\chi 1}}+|\chi_2|^{1+a_{\chi 1}}+|\chi_3|^{1+a_{\chi 1}}\right)-k_{\chi 2}L_\chi\left(|\chi_1|^{1+a_{\chi 2}}+|\chi_2|^{1+a_{\chi 2}}+|\chi_3|^{1+a_{\chi 2}}\right)+\left|\boldsymbol{\chi}^T\boldsymbol{g}_\omega M\right|\end{aligned} \tag{32}$$

In short, $\dot{V}_1 \le 0$ when suitable parameters $K_{\chi i}\,(i=1,2)$ are chosen, indicating that the auxiliary variable $\boldsymbol{\chi}$ is bounded.

Theorem 3. *The proposed NN-ABC scheme can ensure that the tracking errors $\boldsymbol{z_1}$ and $\boldsymbol{z_2}$ are uniformly bounded, which is composed of the RBFNN disturbance observers described by (15), (23) and (28), of the anti-saturation compensator described by (19) and of the backstepping controllers described by (22) and (27).*

Proof.

- The Lyapunov function is selected as

$$V=\frac{1}{2}\boldsymbol{z_1}^T\boldsymbol{z_1}+\frac{1}{2}\boldsymbol{y}^T y+\frac{1}{2}trace\left(\tilde{\boldsymbol{W}}_1^T\Gamma_1^{-1}\tilde{\boldsymbol{W}}_1+\tilde{\boldsymbol{W}}_2^T\Gamma_2^{-1}\tilde{\boldsymbol{W}}_2\right). \tag{33}$$

- The derivative of V is expressed as

$$\dot{V}=\boldsymbol{z_1}^T\dot{\boldsymbol{z}}_1+\boldsymbol{y}^T\dot{\boldsymbol{y}}-trace\left(\tilde{\boldsymbol{W}}_1^T\Gamma_1^{-1}\dot{\hat{\boldsymbol{W}}}_1+\tilde{\boldsymbol{W}}_2^T\Gamma_2^{-1}\dot{\hat{\boldsymbol{W}}}_2\right). \tag{34}$$

- Substituting (23), (24), (28) and (29) into (34), we obtain

$$\begin{aligned}\dot{V}&=\boldsymbol{z_1}^T\left(-K_1\boldsymbol{z_1}+\boldsymbol{g}_\Omega\boldsymbol{z_2}+\tilde{\boldsymbol{W}}_1^T\boldsymbol{\Phi}_1(\boldsymbol{\xi}_1)+\boldsymbol{\varepsilon}_1+\tilde{\dot{\boldsymbol{\Omega}}}_c\right)+\boldsymbol{y}^T\left(-K_2\boldsymbol{y}-\boldsymbol{g}_\Omega^T\boldsymbol{z_1}+\tilde{\boldsymbol{W}}_2^T\boldsymbol{\Phi}_2(\boldsymbol{\xi}_2)+\boldsymbol{\varepsilon}_2+\tilde{\dot{\boldsymbol{\omega}}}_c\right)\\ &\quad -trace\left(\tilde{\boldsymbol{W}}_1^T\boldsymbol{\Phi}_1(\boldsymbol{\xi}_1)\boldsymbol{z_1}^T\right)-trace\left(\tilde{\boldsymbol{W}}_2^T\boldsymbol{\Phi}_2(\boldsymbol{\xi}_2)\boldsymbol{y}^T\right)\\ &=-K_1\boldsymbol{z_1}^T\boldsymbol{z_1}-K_2\boldsymbol{y}^T y+\boldsymbol{z_1}^T\boldsymbol{g}_\Omega\boldsymbol{z_2}-\boldsymbol{y}^T\boldsymbol{g}_\Omega^T\boldsymbol{z_1}+\boldsymbol{z_1}^T\tilde{\boldsymbol{W}}_1^T\boldsymbol{\Phi}_1(\boldsymbol{\xi}_1)+\boldsymbol{z_1}^T\boldsymbol{\varepsilon}_1+\boldsymbol{z_1}^T\tilde{\dot{\boldsymbol{\Omega}}}_c+\boldsymbol{y}^T\tilde{\boldsymbol{W}}_2^T\boldsymbol{\Phi}_2(\boldsymbol{\xi}_2)\\ &\quad +\boldsymbol{y}^T\boldsymbol{\varepsilon}_2+\boldsymbol{y}^T\tilde{\boldsymbol{\omega}}_c-trace\left(\tilde{\boldsymbol{W}}_1^T\boldsymbol{\Phi}_1(\boldsymbol{\xi}_1)\boldsymbol{z_1}^T\right)-trace\left(\tilde{\boldsymbol{W}}_2^T\boldsymbol{\Phi}_2(\boldsymbol{\xi}_2)\boldsymbol{y}^T\right)\\ &=-K_1\boldsymbol{z_1}^T\boldsymbol{z_1}-K_2\boldsymbol{y}^T y+\boldsymbol{z_1}^T\boldsymbol{g}_\Omega\boldsymbol{z_2}-(\boldsymbol{z_2}-\boldsymbol{\chi})^T\boldsymbol{g}_\Omega^T\boldsymbol{z_1}+\boldsymbol{z_1}^T\boldsymbol{\varepsilon}_1+\boldsymbol{z_1}^T\tilde{\dot{\boldsymbol{\Omega}}}_c+\boldsymbol{y}^T\boldsymbol{\varepsilon}_2+\boldsymbol{y}^T\tilde{\dot{\boldsymbol{\omega}}}_c\\ &=-K_1\boldsymbol{z_1}^T\boldsymbol{z_1}-K_2\boldsymbol{y}^T y+\boldsymbol{\chi}^T\boldsymbol{g}_\Omega^T\boldsymbol{z_1}+\boldsymbol{z_1}^T\boldsymbol{\varepsilon}_1+\boldsymbol{z_1}^T\tilde{\dot{\boldsymbol{\Omega}}}_c+\boldsymbol{y}^T\boldsymbol{\varepsilon}_2+\boldsymbol{y}^T\tilde{\dot{\boldsymbol{\omega}}}_c\end{aligned} \tag{35}$$

where

$$\boldsymbol{\chi}^T\boldsymbol{g}_\Omega^T\boldsymbol{z_1}=\begin{bmatrix}\chi_1 & \chi_2 & \chi_3\end{bmatrix}\begin{bmatrix}-\tan\beta\cos\alpha & \sin\alpha & \sec\beta\cos\alpha\\ 1 & 0 & 0\\ -\tan\beta\sin\alpha & -\cos\alpha & \sec\beta\sin\alpha\end{bmatrix}\begin{bmatrix}z_{11} & z_{12} & z_{13}\end{bmatrix}^T. \tag{36}$$

It should be noted that for the bank-to-turn (BTT) scheme, the sideslip angle should be kept near zero [38]. Therefore, we obtain

$$\begin{aligned}\boldsymbol{\chi}^T\boldsymbol{g}_\Omega^T\boldsymbol{z_1}&=\begin{bmatrix}\chi_1 & \chi_2 & \chi_3\end{bmatrix}\begin{bmatrix}0 & \sin\alpha & \cos\alpha\\ 1 & 0 & 0\\ 0 & -\cos\alpha & \sin\alpha\end{bmatrix}\begin{bmatrix}z_{11} & z_{12} & z_{13}\end{bmatrix}^T.\\ &=z_{11}\chi_2+z_{12}(\chi_1\sin\alpha-\chi_3\cos\alpha)+z_{13}(\chi_1\cos\alpha+\chi_3\sin\alpha)\\ &\le |z_{11}|\,|\chi_2|+|z_{12}|\,|\chi_1|+|z_{12}|\,|\chi_3|+|z_{13}|\,|\chi_1|+|z_{13}|\,|\chi_3|\\ &\le \frac{z_{11}^2+\chi_2^2}{2}+\frac{z_{12}^2+\chi_1^2}{2}+\frac{z_{12}^2+\chi_3^2}{2}+\frac{z_{13}^2+\chi_1^2}{2}+\frac{z_{13}^2+\chi_3^2}{2}\\ &=\frac{z_{11}^2}{2}+\frac{\chi_2^2}{2}+z_{12}^2+\chi_1^2+z_{13}^2+\chi_3^2.\end{aligned} \tag{37}$$

https://doi.org/10.1017/aer.2025.10121 Published online by Cambridge University Press

According to **Theorem 1** and **Remark 1**, the estimated errors of $\dot{\tilde{\boldsymbol{\Omega}}}_c$, $\dot{\tilde{\boldsymbol{\omega}}}_c$, $\boldsymbol{\varepsilon}_1$ and $\boldsymbol{\varepsilon}_2$ are bounded. Therefore, the following inequality can be derived

$$\boldsymbol{z}_1^T\tilde{\boldsymbol{\Omega}}_c+\boldsymbol{y}^T\tilde{\boldsymbol{\omega}}_c+\boldsymbol{z}_1^T\boldsymbol{\varepsilon}_1+\boldsymbol{y}^T\boldsymbol{\varepsilon}_2\le\boldsymbol{z}_1^T\boldsymbol{z}_1+\boldsymbol{y}^T\boldsymbol{y}+\frac{\tilde{\boldsymbol{\Omega}}_c^T\tilde{\boldsymbol{\Omega}}_c}{2}+\frac{\tilde{\boldsymbol{\omega}}_c^T\tilde{\boldsymbol{\omega}}_c}{2}+\frac{\boldsymbol{\varepsilon}_1^T\boldsymbol{\varepsilon}_1}{2}+\frac{\boldsymbol{\varepsilon}_2^T\boldsymbol{\varepsilon}_2}{2}. \tag{38}$$

- Substituting (37) and (38) into (35), we obtain

$$\begin{aligned}\dot{V}&\le-K_1\boldsymbol{z}_1^T\boldsymbol{z}_1-K_2\boldsymbol{y}^T\boldsymbol{y}+\frac{z_{11}^2}{2}+\frac{\chi_2^2}{2}+z_{12}^2+\chi_1^2+z_{13}^2+\chi_3^2+\boldsymbol{z}_1^T\boldsymbol{z}_1+\boldsymbol{y}^T\boldsymbol{y}\\&+\frac{\tilde{\boldsymbol{\Omega}}_c^T\tilde{\boldsymbol{\Omega}}_c}{2}+\frac{\tilde{\boldsymbol{\omega}}_c^T\tilde{\boldsymbol{\omega}}_c}{2}+\frac{\boldsymbol{\varepsilon}_1^T\boldsymbol{\varepsilon}_1}{2}+\frac{\boldsymbol{\varepsilon}_2^T\boldsymbol{\varepsilon}_2}{2}\\&=-\left(K_1-\frac{3}{2}\right)z_{11}^2-(K_1-2)\,z_{12}^2-(K_1-2)\,z_{13}^2-(K_2-1)\,y_1^2-(K_2-1)\,y_2^2\\&-(K_2-1)\,y_3^2+\frac{\chi_2^2}{2}+\chi_1^2+\chi_3^2+\frac{\tilde{\boldsymbol{\Omega}}_c^T\tilde{\boldsymbol{\Omega}}_c}{2}+\frac{\tilde{\boldsymbol{\omega}}_c^T\tilde{\boldsymbol{\omega}}_c}{2}+\frac{\boldsymbol{\varepsilon}_1^T\boldsymbol{\varepsilon}_1}{2}+\frac{\boldsymbol{\varepsilon}_2^T\boldsymbol{\varepsilon}_2}{2}\\&\le-(K_1-2)\,\boldsymbol{z}_1^T\boldsymbol{z}_1-(K_2-1)\,\boldsymbol{y}^T\boldsymbol{y}+\frac{\chi_2^2}{2}+\chi_1^2+\chi_3^2+\frac{\dot{\tilde{\boldsymbol{\Omega}}}_c^T\dot{\tilde{\boldsymbol{\Omega}}}_c}{2}+\frac{\dot{\tilde{\boldsymbol{\omega}}}_c^T\dot{\tilde{\boldsymbol{\omega}}}_c}{2}+\frac{\boldsymbol{\varepsilon}_1^T\boldsymbol{\varepsilon}_1}{2}+\frac{\boldsymbol{\varepsilon}_2^T\boldsymbol{\varepsilon}_2}{2}\\&\le-\kappa V+C\end{aligned}, \tag{39}$$

where $K_1>2$, $K_2>1$, $\kappa=\min(K_1-2,K_2-1)$, and

$$C=\frac{\chi_2^2}{2}+\chi_1^2+\chi_3^2+\frac{\dot{\tilde{\boldsymbol{\Omega}}}_c^T\dot{\tilde{\boldsymbol{\Omega}}}_c}{2}+\frac{\dot{\tilde{\boldsymbol{\omega}}}_c^T\dot{\tilde{\boldsymbol{\omega}}}_c}{2}+\frac{\boldsymbol{\varepsilon}_1^T\boldsymbol{\varepsilon}_1}{2}+\frac{\boldsymbol{\varepsilon}_2^T\boldsymbol{\varepsilon}_2}{2}. \tag{40}$$

Recalling **Theorem 2,** $\boldsymbol{\chi}$ is bounded, and C is also bounded.
By setting $\kappa>C/V$, $\dot{V}<0$ can be guaranteed. In this way, the solution of (39) is expressed as

$$0\le V(t)\le\left(V(0)-\frac{C}{\kappa}\right)e^{-\kappa t}+\frac{C}{\kappa}. \tag{41}$$

- Invoking (33) and (41), we have

$$\begin{aligned}\|\boldsymbol{z}_1\|&\le\sqrt{\tfrac{2C}{\kappa}+2\left(V(0)-\tfrac{C}{\kappa}\right)e^{-\kappa t}},\quad\forall t>0\\\|y\|&\le\sqrt{\tfrac{2C}{\kappa}+2\left(V(0)-\tfrac{C}{\kappa}\right)e^{-\kappa t}},\quad\forall t>0\end{aligned}. \tag{42}$$

According to (42), we have $\boldsymbol{z}_1\le\sqrt{2C/\kappa}$, $y\le\sqrt{2C/\kappa}$ as $t\to\infty$. The result of analysis is that the tracking errors $\boldsymbol{z}_1$ and y are uniformly ultimately bounded when correct parameters $\mathbf{K}_i$ $(i=1,2)$ are selected. Furthermore, since $\boldsymbol{z}_2=y+\chi$ and $\boldsymbol{\chi}$ is bounded, it follows that z_2 is also bounded. This is thereby certified.

4.0 Simulation

In this section, we employ Simulink to conduct two comparative experiments. Each experiment comprises a single simulation and a Monte Carlo simulation, aimed to demonstrate the performance of the proposed RBFNNDO and NN-ABC controller. The single simulation provides a focused assessment of

https://doi.org/10.1017/aer.2025.10121 Published online by Cambridge University Press

the controllers' and observers' capabilities under specific conditions, while the Monte Carlo simulation offer an evaluation of the robust performance of the observer and controller in the face of uncertain aerodynamic conditions.

The geometric characteristics of the HFV are demonstrated in Ref. (35). The initial conditions are set as $H = 27.5\text{km}$, $V_b = 2.8 \times 10^3 m/s$, $\alpha = -1^\circ$, $\beta = 0.1^\circ$, $\mu = 0^\circ$ and $p = q = r = 0^\circ/s$. The flow angle commands $\boldsymbol{\Omega}_c$ are selected as $\alpha_c = 2\sin(0.25\pi t)^\circ$, $\beta_c = 0^\circ$, $\mu_c = \sin(0.25\pi t)^\circ$. The external disturbances terms in are presented as $d_\alpha = 0.02\sin(0.25\pi t)\ rad/s$, $d_\beta = 0.01\sin(0.35\pi t) rad/s$, $d_\mu = 0 rad/s$, $d_p = 0.03\sin(0.35\pi t) N \cdot m$, $d_q = 0.04\sin(0.25\pi t)\ N \cdot m$, $d_r = 0.01\sin(0.35\pi t)\ N \cdot m$. The actuators limitations are $-30^\circ \le \delta_a, \delta_e \le 30^\circ$ and $-20^\circ \le \delta_r \le 20^\circ$. The node number of each RBFNN in (15) are 9, the initial weights $\hat{\boldsymbol{W}}_1$ and $\hat{\boldsymbol{W}}_2$ are 0, the RBFNN Gaussian function widths b_{1i} and b_{2i} $(i = 1, 2, \ldots, 9)$ are 0.25 and 0.075 respectively, the RBFNN Gaussian function centres σ_1 and σ_2 are set as

$$\sigma_1 = \begin{bmatrix} -1 & -0.75 & -0.5 & -0.25 & 0 & 0.25 & 0.5 & 0.75 & 1 \\ -0.1 & -0.075 & -0.05 & -0.025 & 0 & 0.025 & 0.05 & 0.075 & 0.1 \\ -0.2 & -0.15 & -0.1 & -0.05 & 0 & 0.05 & 0.1 & 0.15 & 0.2 \\ -2 & -1.5 & -1 & -0.5 & 0 & 0.5 & 1 & 1.5 & 2 \\ -1 & -0.75 & -0.5 & -0.25 & 0 & 0.25 & 0.5 & 0.75 & 1 \\ -2 & -1.5 & -1 & -0.5 & 0 & 0.5 & 1 & 1.5 & 2 \\ -2 & -1.5 & -1 & -0.5 & 0 & 0.5 & 1 & 1.5 & 2 \\ -0.1 & -0.075 & -0.05 & -0.025 & 0 & 0.025 & 0.05 & 0.075 & 0.1 \\ -1 & -0.75 & -0.5 & -0.25 & 0 & 0.25 & 0.5 & 0.75 & 1 \end{bmatrix}, \tag{43}$$

$$\sigma_2 = \begin{bmatrix} -1 & -0.75 & -0.5 & -0.25 & 0 & 0.25 & 0.5 & 0.75 & 1 \\ -1 & -0.75 & -0.5 & -0.25 & 0 & 0.25 & 0.5 & 0.75 & 1 \\ -0.1 & -0.075 & -0.05 & -0.025 & 0 & 0.025 & 0.05 & 0.075 & 0.1 \\ -2 & -1.5 & -1 & -0.5 & 0 & 0.5 & 1 & 1.5 & 2 \\ -1 & -0.75 & -0.5 & -0.25 & 0 & 0.25 & 0.5 & 0.75 & 1 \\ -2 & -1.5 & -1 & -0.5 & 0 & 0.5 & 1 & 1.5 & 2 \\ -2 & -1.5 & -1 & -0.5 & 0 & 0.5 & 1 & 1.5 & 2 \\ -0.1 & -0.075 & -0.05 & -0.025 & 0 & 0.025 & 0.05 & 0.075 & 0.1 \\ -1 & -0.75 & -0.5 & -0.25 & 0 & 0.25 & 0.5 & 0.75 & 1 \end{bmatrix}. \tag{44}$$

4.1 Comparison of RBFNNDO and ESDO

4.1.1 Single simulation

In this subsection, we conduct a comparative analysis of the performance of two observers designed to estimate the lumped disturbances. One uses the RBFNNDO that contains the AFAC, whereas the other uses the ESDO with the rest parts remain identical. The aerodynamic uncertainties in (4) are set as $\Delta C_L = 0.2C_L$, $\Delta C_Y = 0.2C_Y$, $\Delta C_l = 0.2C_l$, $\Delta C_m = 0.2C_m$, $\Delta C_n = 0.2C_n$, and they are unknown to the control law. The parameters of the RBFNNDO are listed out in Table 1, the parameters of the ESDO are listed out in Table 2, and the simulation results are presented in Figs 2 and 3.

$$\begin{cases} \boldsymbol{E}_1 = \hat{\boldsymbol{z}}_{11} - \boldsymbol{\Omega} \\ \dot{\hat{\boldsymbol{z}}}_{11} = f_{\boldsymbol{\Omega}} + \boldsymbol{g}_{\boldsymbol{\Omega}}\boldsymbol{\omega} - \boldsymbol{\eta}_{\boldsymbol{\Omega}1} sig^{0.5}(\boldsymbol{E}_1) + \hat{\boldsymbol{z}}_{12} \\ \dot{\hat{\boldsymbol{z}}}_{12} = -\eta_{\boldsymbol{\Omega}2} sign(\boldsymbol{E}_1) \end{cases}$$
$$\begin{cases} \boldsymbol{E}_2 = \hat{\boldsymbol{z}}_{21} - \omega \\ \dot{\hat{\boldsymbol{z}}}_{21} = \boldsymbol{f}_{\omega} + \boldsymbol{g}_{\omega} u - \boldsymbol{\eta}_{\omega 1} sig^{0.5}(\boldsymbol{E}_2) + \hat{\boldsymbol{z}}_{22} \\ \dot{\hat{\boldsymbol{z}}}_{22} = -\eta_{\omega 2} sign(\boldsymbol{E}_2) \end{cases} \tag{45}$$

https://doi.org/10.1017/aer.2025.10121 Published online by Cambridge University Press

Table 1. *NN-ABC controller parameters in simulation 4.1*

Different controller components	Parameters	Values
RBFNNDO described in (23) and (28)	Positive gain matrices Γ_1, Γ_2	$\Gamma_1 = diag(9.5, 15, 10)$, $\Gamma_2 = diag(30, 30, 30)$.
Finite-time tracking differentiators described in (16)	Positive gain coefficients l_1, l_2, l_3, l_4	$l_1 = 20, l_2 = 110,$ $l_3 = 40, l_4 = 360.$
	Fractional exponents $\alpha_1, \alpha_2, \beta_1, \beta_2$	$\alpha_1 = \beta_1 = 0.8,$ $\alpha_2 = \beta_2 = 0.6.$
AFAC described in (19) and (20)	Positive gain coefficients $k_{\chi 1}, k_{\chi 2}, k_{L\chi 1}, k_{L\chi 2}, k_{L\chi 3}, k_{L\chi 4}$	$k_{\chi 1} = k_{\chi 2} = 0.5,$ $k_{L\chi 1} = 90, k_{L\chi 2} = 100,$ $k_{L\chi 3} = k_{L\chi 4} = 2.$
	Fractional exponents $a_{\chi 1}, a_{\chi 2}, a_{L\chi 1}, a_{L\chi 2}$	$a_{\chi 1} = 0.7, a_{\chi 2} = 1.3,$ $a_{L\chi 1} = 1.5, a_{L\chi 2} = 0.5.$
	The initial value L_{χ_0} and the bounds P^U and P^L of the auxiliary variable L_χ	$L_{\chi_0} = 5, P^U = 10,$ $P^L = 0.6.$
Backstepping controller described in (22) and (27)	Positive gain matrices K_1, K_2	$K_1 = diag(10, 10, 10)$, $K_2 = diag(25, 20, 15)$.

Table 2. *Parameters of ESDO in simulation 4.1*

Different controller components	Parameters	Values
ESDO in (45)	Observer gain matrices $\eta_{\Omega 1}$ $\eta_{\Omega 2}, \eta_{\omega 1}, \eta_{\omega 2}$	$\eta_{\Omega 1} = \eta_{\omega 1} = 0.5I_3, \eta_{\Omega 2} =$ $\text{diag}\left(0.025\ 0.008\ 0.001\right),$ $\eta_{\omega 2} = \text{diag}\left(0.03\ 0.04\ 0.01\right).$

where $\hat{z}_{11}$ and $\hat{z}_{21}$ denote the approximations of the attitude angle $\boldsymbol{\Omega}$ and angular rate ω,respectively; $\hat{z}_{12}$ and $\hat{z}_{22}$ denote the approximations of the lumped disturbances $\boldsymbol{\Delta}_{\boldsymbol{\Omega}}$ and $\boldsymbol{\Delta}_{\boldsymbol{\omega}}$, respectively; $\boldsymbol{\eta}_{\boldsymbol{\Omega} i}$ and $\boldsymbol{\eta}_{\boldsymbol{\omega} i}$ $(i = 1, 2)$ are the observer positive definite diagonal parameter matrix to be designed.

Figures 2 and 3 demonstrate observational errors of the flow angles disturbances and angular rates disturbances in different scenarios, respectively. The specific data analysing of observational performances are listed out in Table 3. During the second phase (when $t > 1.7$s), the maximum values of observational error $\tilde{\Delta}_\mu$ of the two observers are comparable, other observational errors are lower than those for the EDSO-ABC when the proposed RBFNNDO is used. The experimental results confirm the effectiveness of RBFNNDO in approximating complex nonlinear disturbances. However, for simple disturbances such as $d_\mu = 0 rad/s$, ESDO has demonstrated sufficient approximation capability. Considering that disturbances in the real world often exhibit nonlinear characteristics, the RBFNNDO holds greater practical value compared to the ESDO.

4.1.2 Monte Carlo simulation

The results of 200 Monte Carlo simulations are presented to illustrate the robustness of the proposed RBFNNDO. The aerodynamic uncertainties follow a random distribution within the range of ±20% of their baseline values. For simplicity, similar tracking and estimation performance curves are not presented in this subsection. Instead, box plots of the corresponding indexes are drawn to illustrate the effectiveness and robustness of the proposed scheme. The rectangular box of the box plot represents the

https://doi.org/10.1017/aer.2025.10121 Published online by Cambridge University Press

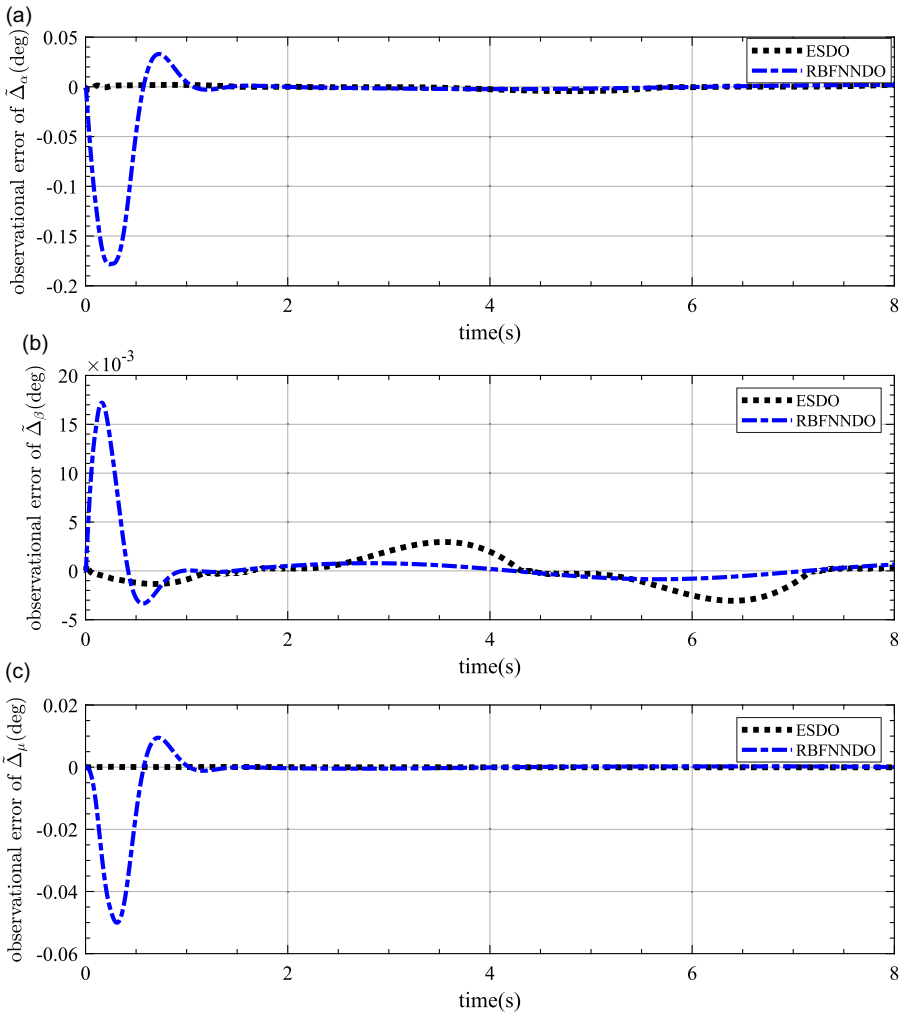


Figure 2. *Observational errors of the flow angles disturbances. (a) Variations of* $\tilde{\Delta}_\alpha$*(b) Variations of* $\tilde{\Delta}_\beta$ *(c) Variations of* $\tilde{\Delta}_\mu$.

middle 50% of the data, the line segment in the middle represents the median of the data, and the long and short whiskers represent the maximum and minimum values of the data.

Figures 4 and 5 demonstrate the maximum observational errors and RMSE of flow angles and angular rates disturbance estimation for different disturbance observers, respectively. The figures clearly show that RBFNNDO has significantly lower average maximum observation errors and RMSE than ESDO under most parameter conditions. Further analysis of the box plots reveals that RBFNNDO also exhibits superior performance, with a more concentrated data distribution and fewer outliers. This indicates that RBFNNDO possesses greater robustness and reliability in handling uncertainties and disturbances.

4.2 Comparison of AFAC and FAC compensators

4.2.1 Single simulation

In this subsection, we conduct a comparative analysis of the performance of two compensators designed to alleviate the effects of input saturation. The first compensator employs an AFAC, while the second

https://doi.org/10.1017/aer.2025.10121 Published online by Cambridge University Press

Table 3. *Comparison of observational performances of RBFFNNDO and ESDO in Simulation 4.1 during the second phase (from $t = 1.7s$ to $t = 8s$)*

	RBFNNDO		ESDO	
Values	Maximum observational errors	RMSE	Maximum observational errors	RMSE
$\tilde{\Delta}_\alpha/^\circ$	1.79×10^{-3}	1.35×10^{-3}	4.15×10^{-3}	2.30×10^{-3}
$\tilde{\Delta}_\beta/^\circ$	6.75×10^{-4}	4.90×10^{-4}	3.02×10^{-3}	1.80×10^{-3}
$\tilde{\Delta}_\mu/^\circ$	3.1×10^{-4}	1.95×10^{-4}	2.90×10^{-4}	1.85×10^{-4}
$\tilde{\Delta}_p/^\circ \bullet s^{-1}$	1.16×10^{-2}	7.67×10^{-3}	1.18×10^{-2}	7.77×10^{-3}
$\tilde{\Delta}_q/^\circ \bullet s^{-1}$	1.05×10^{-2}	7.05×10^{-3}	1.31×10^{-2}	7.35×10^{-3}
$\tilde{\Delta}_r/^\circ \bullet s^{-1}$	8.51×10^{-4}	3.66×10^{-4}	1.63×10^{-3}	5.84×10^{-4}

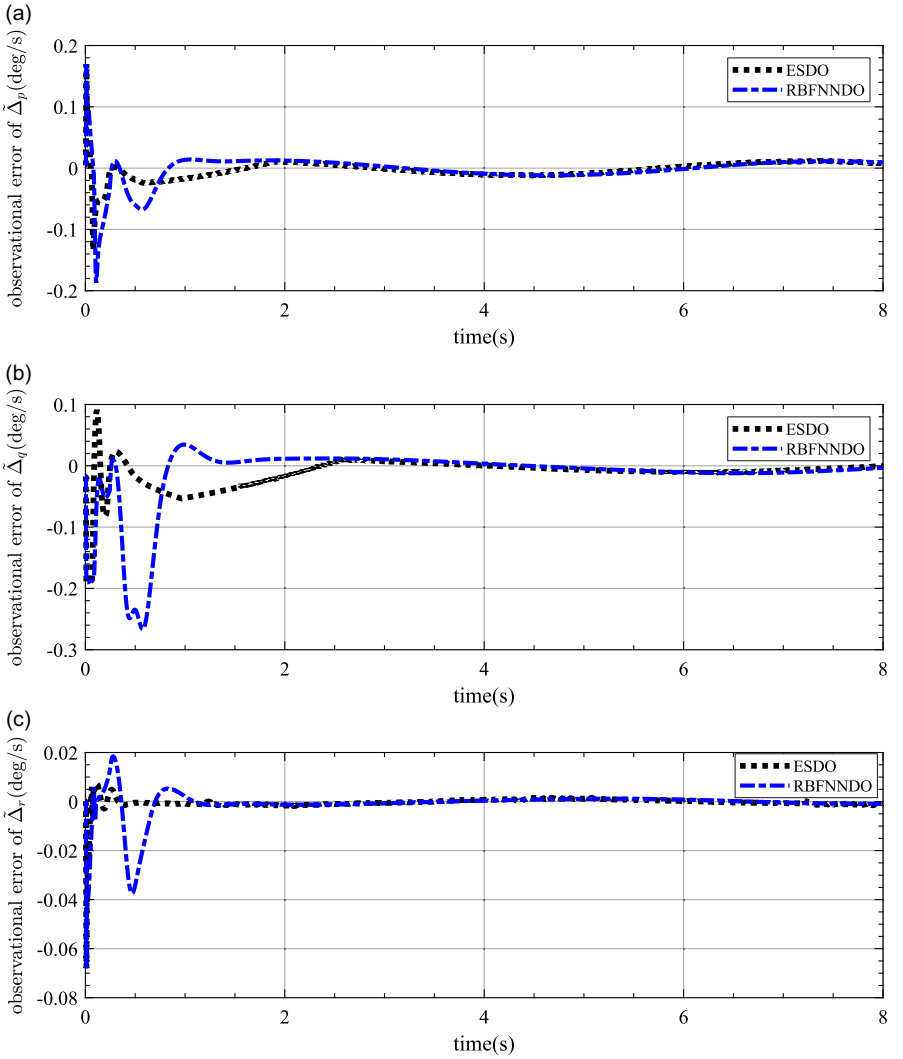


Figure 3. *Observational errors of the angular rates disturbances. (a) Variations of $\tilde{\Delta}_p$ (b) Variations of $\tilde{\Delta}_q$ (c) Variations of $\tilde{\Delta}_r$.*

https://doi.org/10.1017/aer.2025.10121 Published online by Cambridge University Press

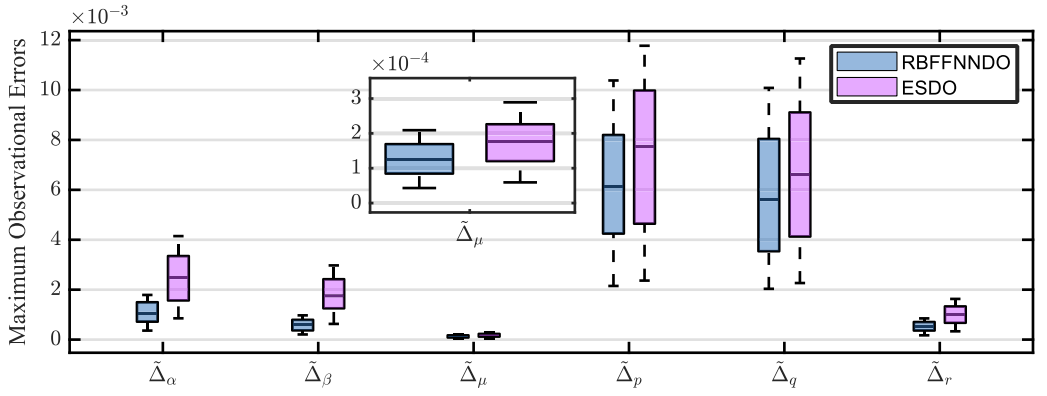


Figure 4. *Comparison of maximum observational errors of RBFFNNDO and ESDO during the second phase (from t = 1.7s to t = 8s).*

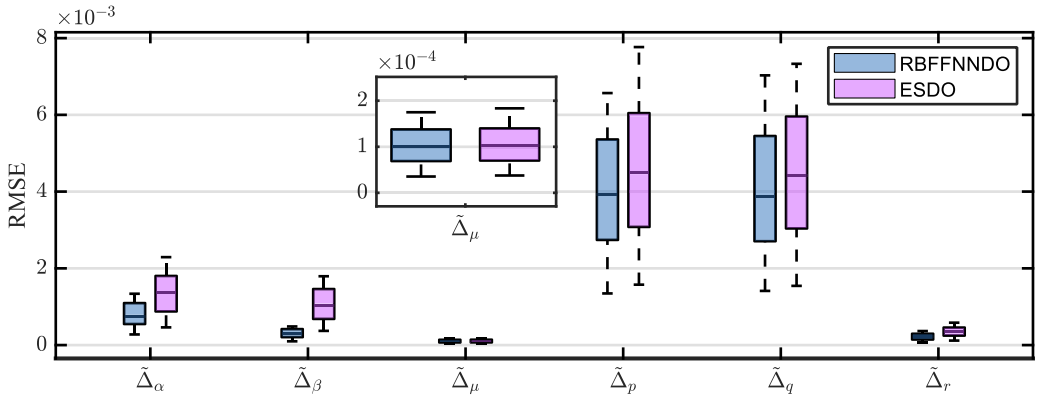


Figure 5. *Comparison of RMSE of RBFFNNDO and ESDO during the second phase (from t = 1.7s to t = 8s).*

utilises the Fixed-Time Anti-Saturation Compensator (FAC) as proposed in Ref. (34). The lumped disturbances are estimated by the RBFNN disturbance observers. The aerodynamic uncertainties in (4) are the same as those set in section 4.1.1.

Therefore, the virtual control law of the NN-FAC is established as

$$\boldsymbol{\omega}_c = \boldsymbol{g}_{\boldsymbol{\Omega}}^{-1}\left(-K_1 \boldsymbol{z}_1 - f_{\boldsymbol{\Omega}} - \hat{\boldsymbol{W}}_1^T \boldsymbol{\Phi}_1\left(\boldsymbol{\xi}_1\right) + \lambda_1\right), \tag{46}$$

Furthermore, the control input $\boldsymbol{u}_c$ of the NN-FAC is designed as

$$\boldsymbol{u}_c = \boldsymbol{g}_{\boldsymbol{\omega}}{}^{-1}\left[-K_2 y - \boldsymbol{g}_{\boldsymbol{\Omega}}^T \boldsymbol{z}_1 - \boldsymbol{f}_{\boldsymbol{\omega}} - \hat{W}_2^T \boldsymbol{\Phi}_2\left(\boldsymbol{\xi}_2\right) + \boldsymbol{\lambda}_2 - \dot{\boldsymbol{\chi}}\right], \tag{47}$$

The anti-saturation compensator is designed according to Ref. (31) and expressed as

$$\dot{\boldsymbol{\chi}} = -k_{\chi 1} \boldsymbol{\chi}^{a_{\chi 1}} - k_{\chi 2} \boldsymbol{\chi}^{a_{\chi 2}} + \boldsymbol{g}_{\boldsymbol{\omega}} \boldsymbol{\Delta} u. \tag{48}$$

The parameters of the NN-ABC controller are listed in Table 1. The parameters of the NN-FAC controller are listed in Table 4, maintaining consistency in the controller parameters with those of the NN-ADSC controller. The simulation outcomes are displayed from Figs 6 through 12.

Figures 6 and 7 demonstrate tracking performances and tracking errors of the flow angles in different scenarios, respectively. The specific data analysing tracking errors and settling time are listed in

https://doi.org/10.1017/aer.2025.10121 Published online by Cambridge University Press

Table 4. *Parameters of NN-FAC controller in simulation 4.2*

Different controller components	Parameters	Values
Controller described in (46) and (47)	positive gain matrices K_1, K_2	$K_1 = diag(10, 10, 10)$, $K_2 = diag(25, 20, 15)$
FAC described in (48)	positive gain coefficients $k_{\chi 1}$, $k_{\chi 2}$	$k_{\chi 1} = k_{\chi 2} = 0.5$
	fractional exponents $a_{\chi 1}$, $a_{\chi 2}$	$a_{\chi 1} = 0.7$, $a_{\chi 2} = 1.3$.

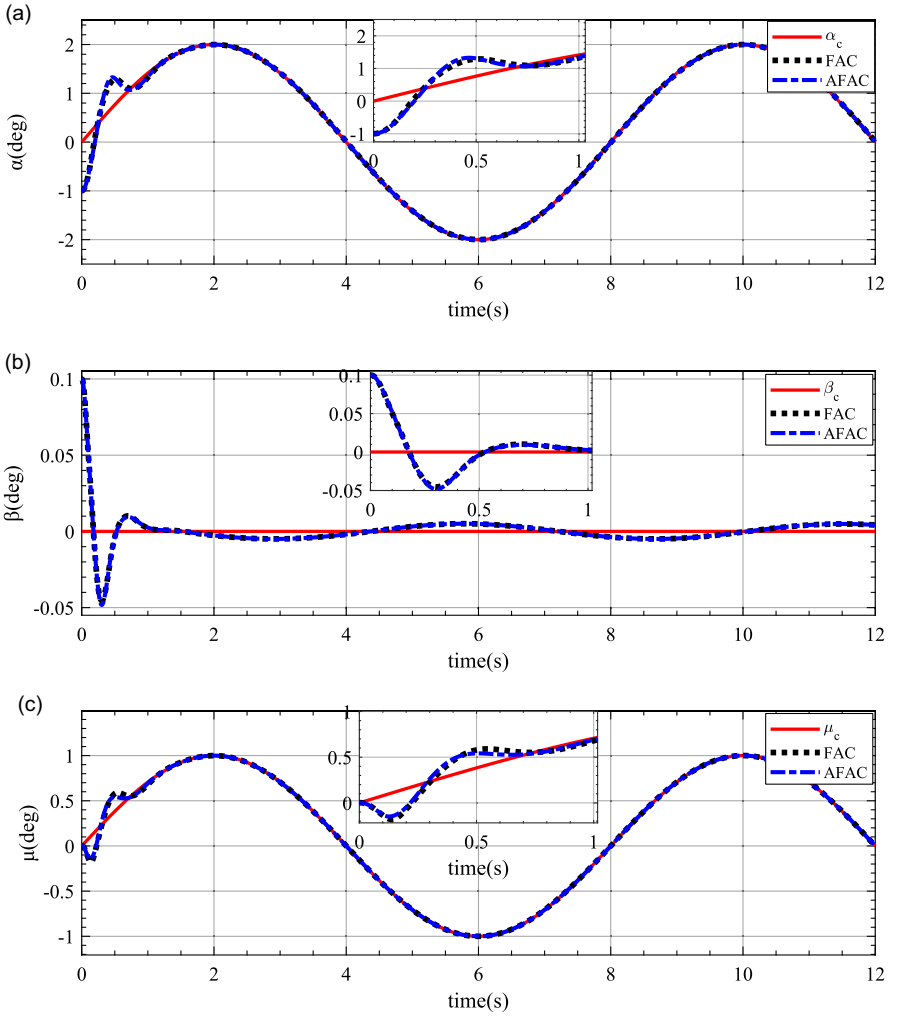


Figure 6. *Tracking performances of the flow angles. (a) Variations of α (b) Variations of β (c) Variations of μ.*

Table 5 and Table 6. During the second phase (when $t > 1.7$s), the maximum values of tracking errors e_α and e_μ are respectively 8.8% and 7.9% lower than those for the NN-FAC when the proposed AFAC is used. It can be observed that the convergence rate and tracking accuracy of our proposed NN-ABC controller outperform those of the NN-FAC controller.

Figures 8 and 9 demonstrate tracking performances and tracking errors of the angular rates in different scenarios, respectively. The specific data analysing tracking performance are listed in Table 7. During the

https://doi.org/10.1017/aer.2025.10121 Published online by Cambridge University Press

Table 5. *Comparison of flow angles tracking performances of AFAC and FAC in simulation 4.2 during the second phase (from t = 1.7s to t = 12s)*

	AFAC		FAC	
Values	Maximum tracking errors	RMSE	Maximum tracking errors	RMSE
$\alpha/^\circ$	1.13×10^{-2}	7.95×10^{-3}	1.14×10^{-2}	7.96×10^{-3}
$\beta/^\circ$	4.92×10^{-3}	3.53×10^{-3}	4.92×10^{-3}	3.53×10^{-3}
$\mu/^\circ$	2.52×10^{-4}	1.45×10^{-4}	2.54×10^{-4}	1.51×10^{-4}

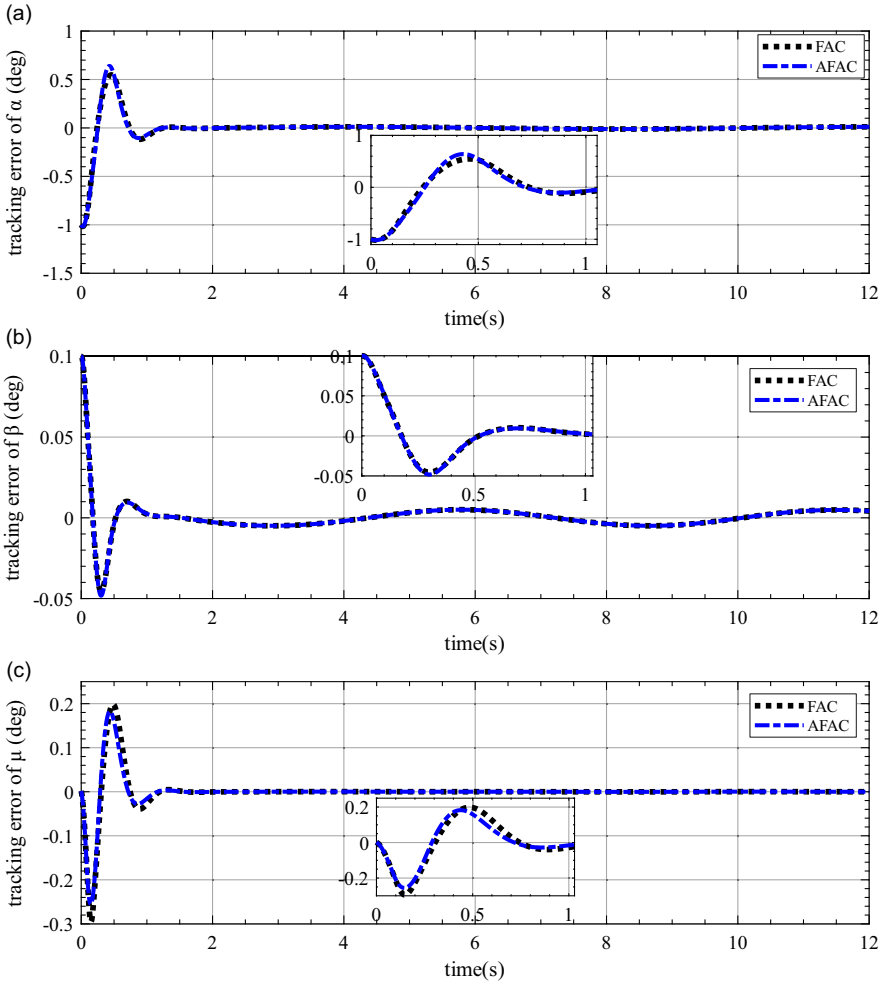


Figure 7. *Tracking errors of the flow angles. (a) Variations of e_α (b) Variations of e_β (c) Variations of e_μ.*

second phase (when $t > 1.7$s), the maximum values of tracking errors*p*, *q*and *r* are respectively 19.4%, 30.8% and 3.8% lower than those for the NN-FAC when the proposed AFAC is used. It can be observed that the convergence rate and tracking accuracy of our proposed NN-ABC controller outperform those of the NN-FAC controller.

Figure 10 demonstrates the comparison variations of the control input, from which it can be observed that the saturation duration decreases when the AFAC is used. The particular data are listed in Table 9.

https://doi.org/10.1017/aer.2025.10121 Published online by Cambridge University Press

Table 6. *Settling time of the flow angles in simulation 4.2*

Values	NN-AFAC	NN-FAC
$\min(\tau)$, *if* $\lvert e_\alpha(t>\tau)/\alpha_c(t>\tau)\rvert < 5\%$	1.275s	1.295s
$\min(\tau)$, *if* $\lvert e_\beta(t>\tau)\rvert < 0.05^\circ$	0.425s	0.425s
$\min(\tau)$, *if* $\lvert e_\mu(t>\tau)/\mu_c(t>\tau)\rvert < 5\%$	1.475s	1.535s

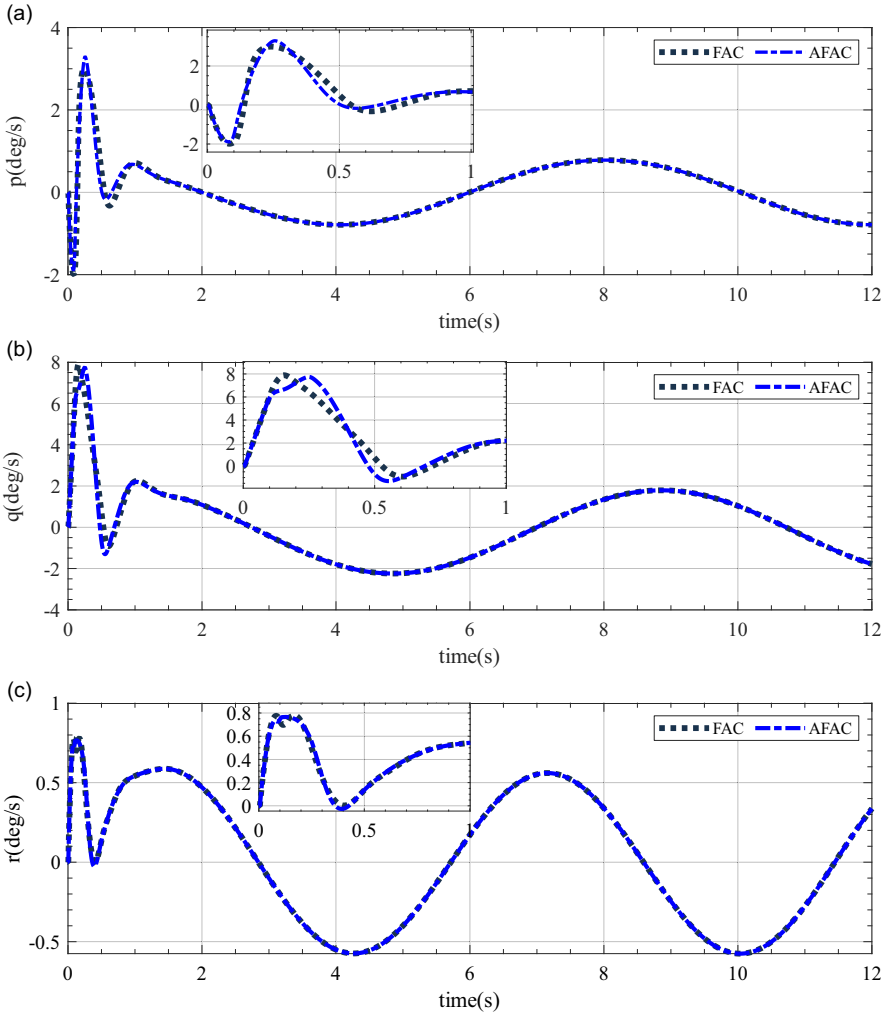


Figure 8. *Variations of angular rates. (a) Variations of p (b) Variations of q (c) Variations of r.*

When the NN-ABC is used, the saturation time of δ_a, δ_e and δ_r are reduced by a minimum of 34.35% compared to the comparative controller. Figures 11 and 12 demonstrate the variations of the auxiliary variable $\boldsymbol{\chi}$ and adaptive parameter L_χ, when the actuator δ_a and δ_e reach saturation, the auxiliary variable $\boldsymbol{\chi}$ begin to decrease, the adaptive parameter L_χ also quickly decreases to an appropriate size, thereby shortening the saturation time of the actuator. When the actuator no longer saturates, the adaptive parameter L_χ rapidly increases, facilitating the rapid convergence of the auxiliary variable $\boldsymbol{\chi}$ to zero.

https://doi.org/10.1017/aer.2025.10121 Published online by Cambridge University Press

Table 7. *Comparison of angular rate tracking performances of AFAC and FAC in simulation 4.2 during the second phase (from t = 1.7s to t = 12s)*

	AFAC		FAC	
Values	Maximum tracking errors	RMSE	Maximum tracking errors	RMSE
$p/^\circ \bullet s^{-1}$	1.00×10^{-2}	6.63×10^{-3}	1.24×10^{-2}	7.23×10^{-3}
$q/^\circ \bullet s^{-1}$	1.01×10^{-2}	6.79×10^{-3}	1.46×10^{-2}	9.28×10^{-3}
$r/^\circ \bullet s^{-1}$	2.79×10^{-3}	2.16×10^{-3}	2.90×10^{-3}	2.18×10^{-3}

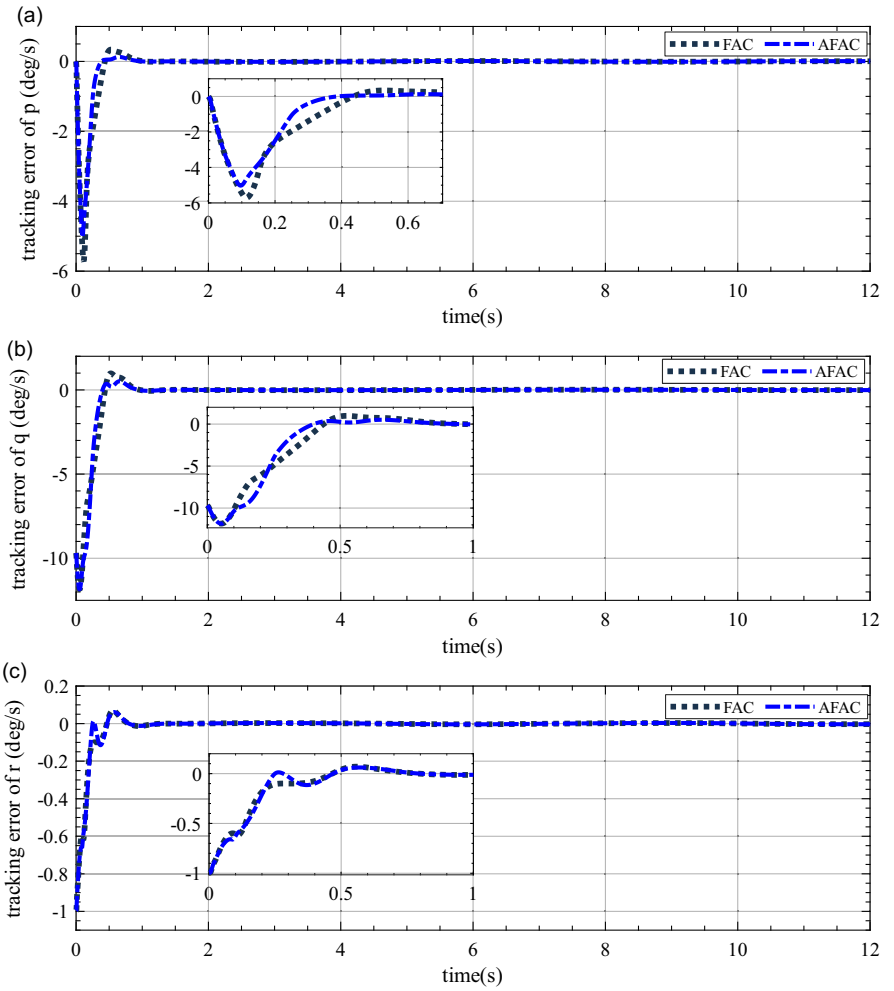


Figure 9. *Tracking performances of the angular rates. (a) Variations of e_p (b) Variations of e_q (c) Variations of e_r.*

4.2.2 Monte Carlo simulation

The results of 200 Monte Carlo simulations are presented to illustrate the robustness of the proposed AFAC. The aerodynamic uncertainties also follow a random distribution within the range of ±20% of their baseline values. Similarly, box plots are drawn to illustrate the effectiveness and robustness of the proposed scheme.

https://doi.org/10.1017/aer.2025.10121 Published online by Cambridge University Press

Table 8. *Settling time of the angular rates in simulation 4.2*

Values	AFAC	FAC
$\min(\tau)$, *if* $\lvert e_p(t>\tau)\rvert < 0.05^\circ/s$	0.810s	0.905s
$\min(\tau)$, *if* $\lvert e_q(t>\tau)\rvert < 0.05^\circ/s$	0.875s	0.905s
$\min(\tau)$, *if* $\lvert e_r(t>\tau)\rvert < 0.05^\circ/s$	0.620s	0.630s

Table 9. *Saturation duration in simulation 4.2*

Saturation duration	AFAC	FAC
δ_a	0.095 s	0.145s
δ_e	0.075 s	0.115s
δ_r	0 s	0 s

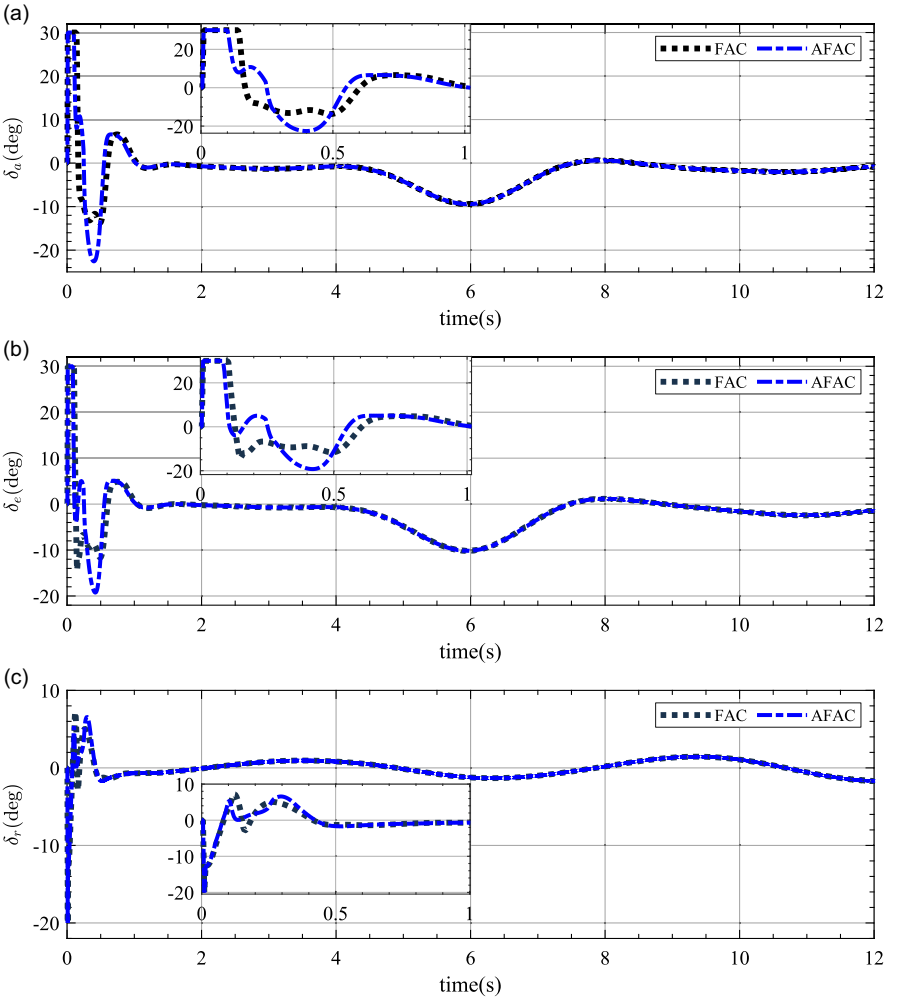


Figure 10. *Variations of the control inputs. (a) Variations of δ_a (b) Variations of δ_e (c) Variations of δ_r.*

https://doi.org/10.1017/aer.2025.10121 Published online by Cambridge University Press

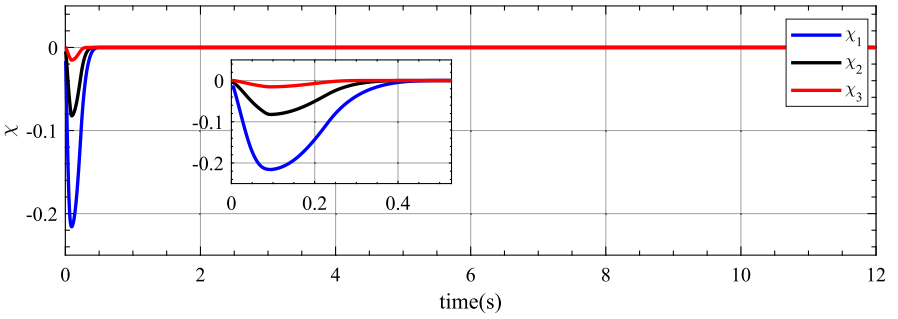


Figure 11. *Variations of the auxiliary variable* $\boldsymbol{\chi}$.

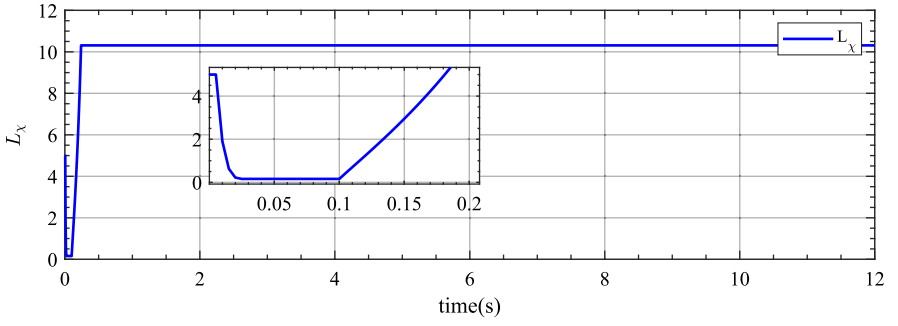


Figure 12. *Variations of the adaptive parameter* L_x.

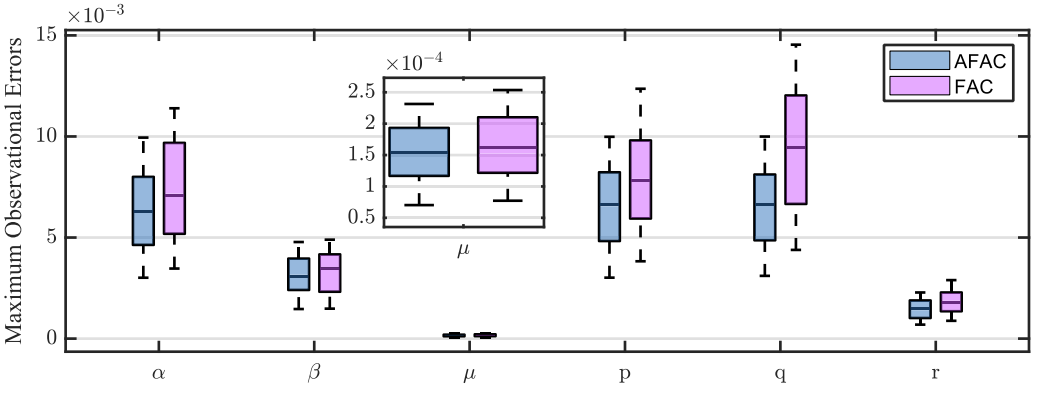


Figure 13. *Comparison of the maximum observational errors of AFAC and FAC during the second phase (from* $t = 1.7s$ *to* $t = 12s$*).*

Figures 13 and 14 demonstrate the maximum tracking errors and RMSE of flow angles and angular rates command tracking using different controllers, respectively. The figures clearly show that AFAC has significantly lower average maximum tracking errors and RMSE than FAC under most parameter conditions. Further analysis of the box plots reveals that AFAC also exhibits superior stability, with a more concentrated data distribution and fewer outliers. This indicates that AFAC possesses greater robustness and reliability in handling uncertainties and disturbances.

https://doi.org/10.1017/aer.2025.10121 Published online by Cambridge University Press

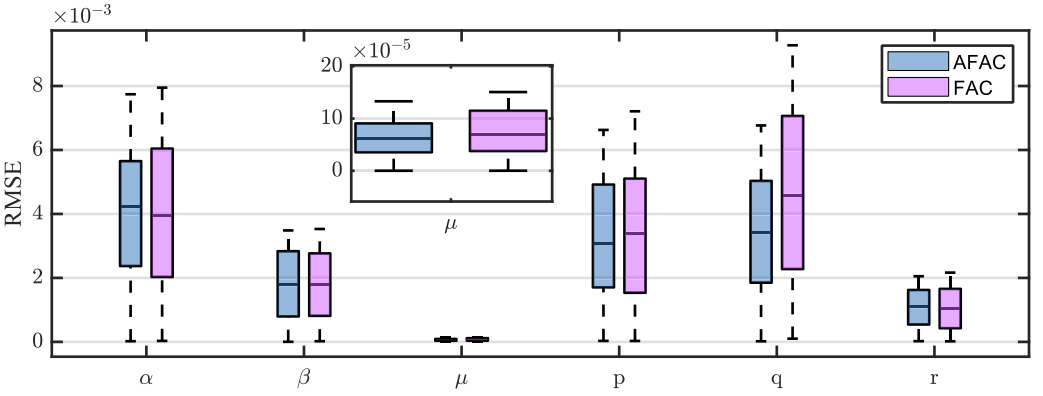


Figure 14. *Comparison of RMSE of AFAC and FAC during the second phase (from t = 1.7s to t = 12s).*

5.0 Conclusions

In this study, we designed a radial basis function neural network disturbance observer based anti-saturation backstepping controller for hypersonic vehicles. This paper adopted finite-time differentiators to address the problem of 'explosion of complexity', achieving higher tracking accuracy and tracking speed. Then, multivariable neural network disturbance observers are designed to estimate the lumped disturbances, by which the robustness of this controller has been greatly improved. In addition, the input saturation issue is dealt with by an adaptive fixed-time anti-saturation compensator that can minimise the saturation duration, and its auxiliary variable rapidly converges to zero after the saturation disappears. The flight control problems for hypersonic flight vehicles under multisource disturbances, and input saturation are systematically solved and analysed.

The simulation results have proven that our proposed controller is superior to the anti-saturation dynamic surface controller in terms of tracking precision, tracking speed and input saturation time. Subsequent research endeavors will employ wind tunnel experiments to replicate critical flight manoeuvres. The objective is to document the model's control response, conduct a rigorous analysis of the data to evaluate the precision of the control algorithm and refine the algorithm based on empirical outcomes. This process is aimed at guaranteeing the algorithm's efficacy and robustness for integration into actual flight control systems.

Future research endeavors will utilise wind tunnel experiments to replicate critical flight manoeuvres. The primary objective is to document the control response of the model, perform a rigorous and detailed analysis of the acquired data to meticulously evaluate the precision and accuracy of this study proposed control algorithm and subsequently refine and optimise the algorithm based on empirical outcomes and insights. This iterative process is designed to ensure the algorithm's efficacy, robustness and reliability, thereby facilitating its integration into actual flight control systems.

Acknowledgements. This work was supported in part by the National Natural Science Foundation of China (Grant No. 62303363) and in part by the China National Postdoctoral Program for Innovative Talents (Grant No. BX20230278).

Data availability statement. The data used to support the findings of this study are included within the article.

Competing interests. The authors declare that they have no conflicts of interest to this work.

References

[1] Ding, Y., Yue, X. and Chen, G. Review of control and guidance technology on hypersonic vehicle, *Chin. J. Aeronaut.*, 2022, **35**, pp 1–18.

[2] Liu, S., Lin, Z., Wang, Y., Huang, W., Yan, B. and Li, Y. Three-body cooperative active defense guidance law with overload constraints: a small speed ratio perspective, *Chin. J. Aeronaut.*, 2025, **38**, p 103171.

https://doi.org/10.1017/aer.2025.10121 Published online by Cambridge University Press

[3] Liu, S., Lin, Z., Huang, W. and Yan, B. Technical development and future prospects of cooperative terminal guidance based on knowledge graph analysis: a review, *J. Zhejiang Univ. Sci. A*, 2025, **34**, pp 605–634.

[4] An, K., Wang, Z., Huang, W. and Liu, S. Performance-prescribed optimal neural control for hypersonic vehicles considering disturbances: an adaptive dynamic programming approach, *Aerosp. Sci. Technol.*, 2024, **152**, p 109370.

[5] Yang, Y., Shao, X. and Shi, Y. Back-stepping robust control for flexible air-breathing hypersonic vehicle via α-filter-based uncertainty and disturbance estimator, *Int. J. Control Autom. Syst.*, 2021, **19**, pp 753–766.

[6] Sartori, D., Quagliotti, F., Rutherford, M.J. and Valavanis, K.P. Design and development of a backstepping controller autopilot for fixed-wing UAVs, *Aeronaut J.*, 2021, **125**, pp 2087–2113.

[7] Wang, J., Zong, Q. and Su, R. Continuous high order sliding mode controller design for a flexible air-breathing hypersonic vehicle, *ISA Trans.*, 2014, **53**, pp 690–698.

[8] Ma, W., Liu, S. and Huang, W. Robust prescribed–time observer–based sliding mode control: theoretical design and flight control applications, ISA Trans., 2025.

[9] Liu, S., Lin, Z., Huang, W. and Yan, B. A new adaptive sliding mode reaching law: theoretical design and simulation analysis, *Adv. Theory Simul.*, 2024, **7**, p 2300736.

[10] Ning, X., Cao, S., Han, B., Wang, Z. and Yin, Y. Adaptive reinforcement learning control for a class of missiles with aerodynamic uncertainties and unmodeled dynamics, *Aeronaut. J.*, 2024, **128**, pp 292–308.

[11] Zhang, H., Wang, P., Tang, G. and Bao, W. Type-2 fuzzy-based fixed-time control for hypersonic morphing vehicles using dual-triggering mechanism, *J. Franklin Inst.*, 2025, **362**, p 107942.

[12] Han, T., Zhang, S., Hu, Q., Shin, H. and Wang, Q. Field-of-view reduced impact angle guidance law via range shaping approach, *IEEE Trans. Aerosp. Electron. Syst.*, 2025, **61**, pp 13090–13106.

[13] Li, W., Wen, Q. and Zhou, H. Adaptive sliding mode formation control for multiple flight vehicles with considering autopilot dynamic, *Aeronaut. J.*, 2021, **125**, pp 1337–1357.

[14] Han, T., Hu, Q., Shin, H., Tsourdos, A. and Xin, M. Incremental twisting fault tolerant control for hypersonic vehicles with partial model knowledge, *IEEE Trans. Ind. Inf.*, 2022, **18**, pp 1050–1060.

[15] Sun, J., Pu, Z. and Yi, J. Fixed-time control with uncertainty and measurement noise suppression for hypersonic vehicles via augmented sliding mode observers, *IEEE Trans. Ind. Inf.*, 2019, **16**, pp 1192–1203.

[16] Zhao, D., Jiang, B. and Yang, H. Backstepping-based decentralized fault-tolerant control of hypersonic vehicles in PDE-ODE form, *IEEE Trans. Autom. Control.*, 2022, **67**, pp 1210–1225.

[17] Xia, J., Zhang, J., Feng, J., Wang, Z. and Zhuang, G. Command filter-based adaptive fuzzy control for nonlinear systems with unknown control directions, *IEEE Trans. Syst. Man Cybern. Syst.*, 2021, **51**, pp 1945–1953.

[18] Farrell, J.A., Polycarpou, M. and Sharma, M. Command Filtered Backstepping, *IEEE Trans. Autom. Control.*, 2009, **54**, pp 1391–1395.

[19] Zhang, X., Zong, Q. and Dou, L. Improved finite-time command filtered backstepping fault-tolerant control for flexible hypersonic vehicle, *J. Franklin Inst.*, 2020, **357**, pp 8543–8565.

[20] Yu, J., Shi, P. and Zhao, L. Finite-time command filtered backstepping control for a class of nonlinear systems, *Automatica*, 2018, **92**, pp 173–180.

[21] Zong, Q., Ji, Y., Zeng, F. and Liu, H. Output feedback back-stepping control for a generic hypersonic vehicle via small-gain theorem, *Aerosp. Sci. Technol.*, 2012, **23**, pp 409–417.

[22] Cheng, X., Wang, P. and Tang, G. Robust attitude control of air-breathing hypersonic vehicles with mismatched disturbances, 36th Chin. Control Conf., Dalian, China, 2017, pp 6489–6494.

[23] Wang, N., Karimi, H.R. and Li, H. Accurate trajectory tracking of disturbed surface vehicles: a finite-time control approach, *IEEE/ASME Trans. Mechatron.*, 2019, **24**, pp 1064–1074.

[24] An, K., Wang, Z., Huang, W. and Liu, S. Performance-prescribed optimal neural control for hypersonic vehicles considering disturbances: An adaptive dynamic programming approach, *Aerosp. Sci. Technol.*, 2024, **152**, p 109370.

[25] Bu, X. and Lei, H. A fuzzy wavelet neural network-based approach to hypersonic flight vehicle direct nonaffine hybrid control, *Nonlinear Dyn.*, 2018, **94**, pp 1657–1668.

[26] Sun, Y., Xu, J. and Wu, H. Deep learning based semi-supervised control for vertical security of maglev vehicle with guaranteed bounded airgap, *IEEE Trans. Intell. Transp. Syst.*, 2021, **22**, pp 4431–4442.

[27] Sun, J. and Song, S. Tracking control of hypersonic vehicles with input saturation based on fast terminal sliding mode, *Int. J. Aeronaut. Space Sci.*, 2019, **20**, pp 493–505.

[28] Dong, C., Liu, Y. and Wang, Q. Barrier Lyapunov function based adaptive finite-time control for hypersonic flight vehicles with state constraints, *ISA Trans.*, 2020, **96**, pp 163–176.

[29] Zhang, D., Ma, P. and Wang, S. Multi-constraints adaptive finite-time integrated guidance and control design, *Aerosp. Sci. Technol.*, 2020, **107**, p 106334.

[30] Bu, X., Wu, X. and Wei, D. Neural-approximation-based robust adaptive control of flexible air-breathing hypersonic vehicles with parametric uncertainties and control input constraints, *Inf. Sci.*, 2016, **346–347**, pp 29–43.

[31] An, H., Liu, J. and Wang, C. Approximate back-stepping fault-tolerant control of the flexible air-breathing hypersonic vehicle, *IEEE/ASME Trans. Mechatron.*, 2016, **21**, pp 1680–1691.

[32] Ding, Y., Yue, X. and Liu, C. Finite-time controller design with adaptive fixed-time anti-saturation compensator for hypersonic vehicle, *ISA Trans.*, 2022, **122**, pp 96–113.

[33] Keshmiri, S., Mirmirani, M.D. and Colgren, R. Six-DOF modeling and simulation of a generic hypersonic vehicle for conceptual design studies, *Proc. AIAA Model. Simul. Technol. Conf.*, Providence, RI, USA, 2004.

[34] Zhao, J., Feng, D. and Cui, J. Finite-time extended state observer-based fixed-time attitude control for hypersonic vehicles, *Math.*, 2022, **10**, p 3162.

https://doi.org/10.1017/aer.2025.10121 Published online by Cambridge University Press

[35] Zhong, Q., Zhao, J. and Liu, R. Disturbance observer–based backstepping control for hypersonic vehicles with input constraints, *J. Aerosp. Eng.*, 2023, **37**, 04023092-1-12.
[36] Zuo, Z., Tie, L. Distributed robust finite-time nonlinear consensus protocols for multi-agent systems, *Int. J. Syst. Sci.*, 2014, **47**, pp 1366–1375.
[37] Wang, X., Guo, J. and Tang, S. Neural network based multivariable fixed-time terminal sliding mode control for reentry vehicles, *IET Control Theory Appl.*, 2018, **12**, pp 1763–1772.
[38] Dai, P., Yan, B. and Han, T. Barrier Lyapunov function based model predictive control of a morphing waverider with input saturation and full-state constraints, *IEEE Trans. Aerosp. Electron. Syst.*, 2023, **59**, pp 3071–3081.
[39] Polyakov, A. Nonlinear feedback design for fixed-time stabilization of linear control systems, *IEEE Trans. Autom. Control*, 2012, **57**, pp 2106–2110.

Cite this article: Wang C., Feng D., Zhao J., Dai P., Chen T. and Wang X. (2026). Neural network disturbance observer-based anti-saturation backstepping control for hypersonic vehicles. *The Aeronautical Journal*, **130**, 1083–1106. https://doi.org/10.1017/aer.2025.10121

https://doi.org/10.1017/aer.2025.10121 Published online by Cambridge University Press